

# Dynamical mass constraints on the ultraluminous X-ray Source NGC 1313 X-2

Jifeng Liu<sup>1,2</sup>, Jerome Orosz<sup>3</sup>, and Joel N. Bregman<sup>4</sup>

## ABSTRACT

Dynamical mass measurements hold the key to answering whether ultraluminous X-ray sources (ULXs) are intermediate mass black holes (IMBHs) or stellar mass black holes with special radiation mechanisms. NGC 1313 X-2 is so far the only ULX with HST light curves, the orbital period, and the black hole's radial velocity amplitude based on the He II  $\lambda 4686\text{\AA}$  disk emission line shift of  $\sim 200$  km/s. We constrain its black hole mass and other parameters by fitting observations to a binary light curve code with accommodations for X-ray heating of the accretion disk and the secondary. Given the dynamical constraints from the observed light curves and the black hole radial motion and the observed stellar environment age, the only acceptable models are those with 40-50 Myrs old intermediate mass secondaries in their helium core and hydrogen shell burning phase filling 40%-80% of their Roche lobes. The black hole can be a massive black hole of a few tens of  $M_{\odot}$  that can be produced from stellar evolution of low metallicity stars, or an IMBH of a few hundred to above  $1000M_{\odot}$  if its true radial velocity  $2K' < 40$  km/s. Further observations are required to better measure the black hole radial motion and the light curves in order to determine whether NGC 1313 X-2 is a stellar black hole or an IMBH.

*Subject headings:* catalogs – galaxies: general – X-rays: binaries – X-rays: galaxies

---

<sup>1</sup>National Astronomical Observatory of China, Beijing, China 100012

<sup>2</sup>Harvard-Smithsonian center for Astrophysics, 60 Garden st. Cambridge, MA 02138

<sup>3</sup>San Diego State University, San Diego, Ca 92182

<sup>4</sup>University of Michigan, Ann Arbor, MI 40185

## 1. INTRODUCTION

Recent X-ray observations have revealed many ultraluminous X-ray sources (ULXs), i.e., non-nuclear point sources in nearby galaxies with X-ray luminosities in the range of  $2 \times 10^{39} - 10^{41} \text{ erg s}^{-1}$  (Fabbiano 1989; Colbert & Mushotzky 1999). Some ULXs may well be foreground stars or background AGN/QSOs projected into the host galaxies (e.g., Gutierrez 2006), or recent supernovae (e.g., SN1993J in M81). Most ULXs, however, should be intermediate mass black holes (IMBHs) of  $100\text{--}10^5 M_{\odot}$  radiating at sub-Eddington levels, or stellar mass black holes with special radiation mechanisms, such as relativistic beaming (Georganopoulos et al. 2002), beaming effects (King et al. 2001) or truly super-Eddington emission from magnetized accretion disks with photon bubbles (Begelman et al. 2002). X-ray spectroscopy and X-ray quasi-periodic oscillation behaviors may support the interpretation for IMBHs for some ULXs (e.g., Strohmayer & Mushotzky 2003; Liu & Di Stefano 2008). However, the X-ray spectra might be explained otherwise such as the very high state of stellar mass black holes under super-critical accretion (Gladstone et al. 2009), and the QPO argument is also inconclusive given our poor understanding of the QPO behaviors.

Whether ULXs are IMBHs can only be securely addressed by measuring their dynamical masses. The dynamical mass measurement is a well-defined process and requires that we (1) identify the secondary unambiguously in the optical and derive the secondary properties, (2) obtain the orbital period  $P$  and the inclination angle  $i$  from the light curve, and (3) measure the radial velocity half-amplitude  $K$  of the secondary with optical spectroscopy. The resulting mass function  $f(M) = PK^3/2\pi G = m_1^3 \sin^3 i / (m_1 + m_2)^2$  will set the lower limit for the black hole mass  $m_1$ . The black hole mass can be further determined if we know the inclination angle  $i$  and the secondary mass  $m_2$ . So far, about 20 ULXs were identified in the optical with unique or multiple counterparts mostly through registering Chandra X-ray positions onto HST images (e.g., Liu et al. 2002, 2004; Roberts et al. 2008). For ULX counterparts, it is impractical to measure the radial velocity with the shallow narrow photospheric absorption lines from the secondary given their optical faintness ( $V \geq 22$  mag) due to their location in distant galaxies. Instead, we must resort to strong emission lines to determine the radial motion.

Strong emission lines can come from the ULX secondary if the secondary is a Wolf-Rayet (WR) star. Most recently, the secondary of M101-ULX1 is identified and spectroscopically confirmed as a WR star with strong He II  $\lambda 4686$  and He I  $\lambda 5876$  emission lines (Liu 2009), and Keck/Gemini spectroscopic monitoring programs (PI: Liu) are under way to determine the radial velocity half-amplitude  $K$  of the secondary and ultimately the black hole mass. However, M101-ULX1 is the only ULX with a WR secondary, and may not be representative of the class. Strong emission lines are expected from the X-ray photoioniza-

tion of the accretion disk for ULXs with high X-ray luminosities above a few  $\times 10^{39}$  erg/s. Indeed, emission lines are observed for low-mass X-ray binaries during outbursts with X-ray luminosities above only a few  $\times 10^{38}$  erg/s. The black hole mass can be derived from  $f'(M) = PK'^3/2\pi G = m_2^3 \sin^3 i / (m_2 + m_1)^2$ , where  $K'$  is the radial velocity semi-amplitude of the black hole as measured from the disk emission lines.

The explanation of the ULX optical observations is complicated by the X-ray irradiation of the accretion disk and the side of the secondary facing the primary, which becomes very significant for ULXs. Indeed, the X-ray irradiated accretion disk can overwhelm the secondary itself by a factor of  $\geq 100$  in X-ray outbursts of Galactic low mass X-ray binaries (van Paradijs & McClintock 1994). Kaaret & Corbel (2009) claimed, based on the spectral slopes and other features of their VLT/FORS spectra, that the optical light from an ULX in NGC 5408 mainly comes from an X-ray irradiated accretion disk. If X-ray irradiation is unimportant, and periodic modulations come from the orbital motion of the binary with its tidally distorted secondary, one expects a smooth ellipsoidal light curve with two maxima and two unequal minima. The deeper minimum comes from the heavily gravitationally darkened side of the secondary close to the L1 point (hereafter the L1 side), the shallower minimum comes from its antipodal side, while the two maxima come from the other two sides. If X-ray heating of the L1 side of the secondary is so significant as to boost it from the darkest to brightest side, then one expects a sinusoidal light curve with one maximum from the X-ray heated side, and one minimum from its antipodal side.

In this work, we describe our efforts to constrain the black hole mass and the secondary simultaneously for NGC 1313 X-2 through the detected light curves and the radial velocity changes of the disk emission line. The light curve for NGC 1313 X-2 is largely sinusoidal with an amplitude of  $\Delta F_{450W} = 0.2$  mag (Liu et al. 2009), and the X-ray irradiation must be significant. The X-ray irradiated binary model used to fit the light curves is described briefly in §2, with details given in the appendix. The constraints on the black hole mass and other parameters are derived based on  $\chi^2$  minimization as described in §3. The results are discussed in §4.

## 2. AN X-RAY IRRADIATED BINARY MODEL

A model with X-ray irradiation properly included should be developed to get dynamical parameters of ULXs from the optical spectra and light curves. In such a black hole binary model, the secondary star should fill a significant part of its tidally distorted pear-like Roche lobe to provide the high accretion rates required by the high X-ray luminosity (King et al. 2001). Many models of close binaries have been developed to model the ellipsoidal

light curves without X-ray irradiation (see the review by Wilson 1994). One example is the eclipsing binary light curve code (ELC; Orosz & Hauschildt 2000), which fits the wide-band photometric light curve and the radial velocity curve to get the dynamical parameters. Copperwheat et al. (2005) developed an X-ray irradiated black hole binary model with the secondary surface approximated as black body emitters, which predicts the wide-band photometry but not the spectrum for ULX optical counterparts. To fully utilize the optical spectroscopic and photometric monitoring observations of ULXs, we have developed a computer code to model both the spectrum and the photometry from the X-ray irradiated black hole binary with the (X-ray heated) secondary described by Kurucz stellar atmospheres.

In constructing the X-ray irradiated close binary model, we described the tidally distorted secondary following Kopal (1954) and Lucy (1967), treated the accretion disk as a standard disk (Shakura & Sunyaev 1973) that can be fattened due to X-ray irradiation, modeled the X-ray heating of the disk and the secondary surface following Frank, King & Raine (2002), and described the X-ray heated secondary following Kurucz stellar atmosphere models. We tried not to just patch up existing code segments, but wrote the computer code in C from scratch. The model construction is detailed in the appendix, so that one can rewrite the code if one so wishes. This model has 10 parameters, including five parameters to set up the binary model without X-ray irradiation: (1) the black hole mass  $M_{\bullet}$ , (2-3) the secondary’s initial mass and age which determine its mass ( $M_*$ ), radius ( $R_*$ ) and temperature ( $T_*$ ), (4) the fraction ( $f_R$ ) the secondary fills its Roche lobe by volume, and (5) the inclination angle  $\Theta$ . Five extra parameters are required to incorporate the X-ray irradiation: (6) the X-ray luminosity  $L_X$ , (7) the disk thickness, as described by a fattening factor  $X_h$  relative to a standard disk, (8) the disk size, as described by a factor  $X_d$  relative to its maximal tidal-disruption radius, (9) the disk albedo  $\beta$ , and (10) the X-ray to thermal conversion factor  $\gamma$  on the X-ray heated secondary surface.

Given the parameters, the model first sets up the binary geometry, computes the secondary and disk temperature profiles with and without X-ray irradiation, then computes the emergent spectrum and the magnitudes for a binary phase  $\Phi$ . For illustration purposes, we put the model output in one figure for one binary phase as shown in Figure 1 for a model with  $M_{\bullet} = 30M_{\odot}$ , a B0V secondary ( $M_* = 17.5M_{\odot}$ ,  $R_* = 7.4R_{\odot}$ , and  $T_* = 30,000$  K with solar abundance) filling its Roche lobe ( $f_R = 1$ ),  $L_X = 10^{39}$  erg s $^{-1}$ ,  $X_h = 1$ ,  $X_d = 0.5$ ,  $\beta = 0.5$ ,  $\gamma = 0.5$ , and  $\Theta = 60^{\circ}$ . The upper left panel shows the binary components projected on the plane normal to the viewing vector, and the upper right panel shows the *UBVRIJHK* light curves for a whole period with the magnitudes marked for this phase. The lower panel shows the emergent spectrum from the secondary with X-ray irradiation and its spectrum without X-ray irradiation, the spectrum from the disk itself and the spectrum with the X-ray irradiation contribution, and the spectrum from the binary as a whole.

### 3. DYNAMICAL PARAMETERS OF NGC 1313 X-2

NGC 1313 X-2 is a ULX with an observed maximum luminosity of  $3 \times 10^{40}$  erg/s (Feng & Kaaret 2006) in a nearby spiral galaxy NGC 1313 at a distance of 3.7 Mpc (Tully 1988). NGC 1313 X-2 has been studied extensively both in the X-ray and the optical to understand its companion and environments. The optical counterpart has been established as a B=23.5 mag blue star through a train of efforts (Zampieri et al. 2004; Mucciarelli et al. 2005; Ramsey et al. 2006; Liu et al. 2007). Optical spectra of its counterpart have shown variable HeII  $\lambda 4686$  emission lines (FWHM=3~10Å) from the accretion disk, and a line shift of  $380 \pm 30$  km/s was detected between two VLT spectroscopic observations (Pakull et al. 2006; Grise et al. 2009). Our HST Cycle 16 GO program monitored this counterpart with 20 WFPC2 B/V observations, and revealed a sinusoid-like light curve with a half-amplitude of  $A_B = 0.102 \pm 0.016$  mag and a period of  $P = 6.12 \pm 0.16$  days (Liu et al. 2009). A slightly shorter period of  $\sim 6$  days is obtained when about a dozen of VLT observations over five months are included (Zampieri et al. 2011). The above information leads to  $f'(M) \geq 4.4/2.4/1.2M_\odot$  if we adopt  $2K' = 380/200/100$  km/s, which sets the lower limit for the secondary mass.

Ten Gemini-S/GMOS follow-up observations were obtained for NGC 1313 X-2 within two months in semester 2009B, which detected the anticipated shift in the He II  $\lambda 4686\text{\AA}$  line with respect to its local vicinity (Roberts et al. 2010; Gladstone et al. 2011). The He II  $\lambda 4686\text{\AA}$  emission line most probably comes from the X-ray irradiated accretion disk, since the underlying continuum of these GMOS spectra is a featureless power-law in resemblance of X-ray irradiated accretion disk like in the case of VLT/FORS spectra for NGC 5408-ULX (Kaaret & Corbel 2009). Unfortunately, there is no evidence for a sinusoidal radial velocity curve, and the data does not provide a new, solid constraint on the mass function for NGC 1313 X-2. Based on the detailed analysis by Gladstone et al. (2011), the  $2\sigma$  rms scatter of the velocity shift is  $182 \pm 40$  km/s. This places an upper limit on the radial velocity change, which enables to constrain the dynamical parameters for NGC 1313 X-2. In §3.1 we constrain the dynamical parameters by assuming  $2K' = 200 \pm 40$  km/s. When using the disk emission line to probe the black hole motion, the observed radial velocity amplitude can be two times higher than the true radial velocity amplitude (Cantrell & Bailyn 2007); we thus run a second case in §3.2 assuming  $2K' = 100 \pm 40$  km/s. We also run a third case in §3.3 assuming  $2K' = 25 \pm 15$  km/s to illustrate how the dynamical parameters change for lower values of  $2K'$ .

### 3.1. In case of $2K' = 200 \pm 40$ km/s

Based on the observed sinusoidal light curves and the black hole’s radial velocity amplitude for NGC 1313, the dynamical parameters, including the black hole mass and the secondary properties, can be derived with the X-ray irradiated binary model as described in §2. For this purpose, we define  $\chi^2 = \sum_i (m_i - m_d)^2/e_i^2 + (P_d - P)^2/\sigma_P^2 + (K'_d - K')^2/\sigma_{K'}^2$ . Here  $m_i$  and  $e_i$  are the observed HST magnitudes and errors,  $P = 6.12$  days and  $\sigma_P = 0.16$  days are the detected period and error (Liu et al. 2009),  $2K' = 200$  km/s and  $\sigma_{K'} = 40$  km/s are the radial velocity semi-amplitude of the black hole and error based on the Gemini observations (Roberts et al. 2010; Gladstone et al. 2011), while  $m_d$  is the predicted magnitude at the observed phase,  $P_d$  and  $K'_d$  are the corresponding quantities predicted by the model. Five F555W observations are excluded from the fit because they exhibited abnormally red colors and abnormally large deviations from the sinusoidal light curve (Liu et al. 2009). The Padova stellar model grid (Girardi et al. 2002), with  $Z=0.1Z_\odot$  as appropriate for NGC 1313 (Ryder 1993), is used to determine the secondary properties with two parameters, the age  $t$  and the initial mass  $m_{ini} = m_f \cdot m_{ini,max}$  with  $m_f$  defined as fraction of the maximum initial mass allowed for that age. In addition to the ten parameters to describe the X-ray irradiated binary model, we assume an extinction  $E(B-V)$  with the standard galactic extinction law to convert model magnitudes to observed magnitudes.

Acceptable models are searched over the 11-parameter phase space by minimizing the above defined  $\chi^2$  with 26 degrees of freedom (37 constraints and 11 free parameters). To not miss any acceptable models, we start with very loose constraints on the parameters, with  $3 < M_\bullet/M_\odot < 3000$ ,  $6.6 < \lg(t) < 8.4$ ,  $0.3 < m_f < 1$ ,  $0.05 < f_R < 1$ ,  $0 < \Theta < 90$ ,  $30 < L_X/10^{38} < 300$ ,  $1 < X_h < 10$ ,  $0.05 < X_d < 0.9$ ,  $0.01 < \beta < 0.99$ ,  $0.01 < \gamma < 0.99$ , and  $0.11 < E(B-V) < 0.44$ . Here the extinction value is bounded within 0.11 mag (Galactic extinction) and 0.44 mag, i.e.,  $n_H = 2.7 \times 10^{21}$  cm $^{-2}$  as inferred from the fit to the X-ray spectrum (Miller et al. 2003). The X-ray luminosity is bounded within  $3 \times$  and  $30 \times 10^{39}$  erg/s with an average of  $\sim 4 \times 10^{39}$  erg/s based on previous X-ray observations (Mucciarelli et al. 2005). The average X-ray luminosity corresponds to an accretion rate of  $\dot{M} = 2 \times 10^{-7} (L/10^{39})(0.1/\eta) \sim 8 \times 10^{-7} M_\odot/\text{yr}$  from  $L_{acc} = \eta \dot{M} c^2$  regardless the black hole mass. Based on the accretion rate consideration, models are discarded unless the secondary is filling ( $> 98\%$  of) its Roche lobe, or the secondary has already evolved off the main sequence into its red/blue giant or asymptotic giant phases and fills a significant fraction of its Roche lobe, so that the heavy stellar winds can be focused onto the primary to provide the required accretion rate.

Given the vast parameter space, the  $\chi^2$  minimization is an extremely difficult problem that demands carefully designed intensive computations, which are carried out using the

Odyssey cluster at Harvard University. As the first step,  $10^8$  models are randomly drawn over the 11-dimension phase space. This is equivalent to an average of  $10^{8/11} \sim 5.3$  sampled values over the parameter range for each dimension, but with the advantage of continuous coverage due to randomization. Most of the  $10^8$  models have extremely large  $\chi^2$  values, including about 20 models with  $\chi^2 < 260$  (i.e.,  $\chi_\nu^2 < 10$ ), and about 25000 models with  $\chi^2 < 10000$ . As shown in Figures 2a-f,  $M_\bullet$ ,  $\Theta$ ,  $\lg(t)$ ,  $m_f$  and E(B-V) are clearly constrained even at the  $\chi^2 < 10000$  level, while  $L_X$ ,  $X_h$ ,  $X_d$ ,  $f_R$ ,  $\beta$  and  $\gamma$  are not constrained. At the  $\chi^2 < 10000$  level, models with black hole masses above  $1000M_\odot$  or inclination angles below  $20^\circ$  are not acceptable. Only certain combinations of the secondary age and initial mass in the two thin stripes are possibly acceptable. Secondaries in the lower stripe are starting the helium core and hydrogen shell burning phase, and secondaries in the upper stripe are starting the carbon core and helium shell burning phase, while all have similar average densities appropriate for the detected orbital period ( $P = \sqrt{110/\rho}$  with  $\rho$  as the mean matter density within the secondary’s Roche lobe; Paczynski 1972). While we start with a uniform distribution of E(B-V) within 0.11 mag and 0.44 mag, it is found that models with larger E(B-V) are more likely to be unacceptable.

Local  $\chi^2$  minima are then searched using the AMOEBA method as described in *Numerical Recipe* (Press et al. 2003) adapted to computing with the Odyssey cluster. Selected as starting points are about 6000 models as shown in Figures 2a-f, including all models with  $\chi^2 < 2000$  and those with lowest  $\chi^2$  within fine intervals of each parameter. This large number of initial guesses provides a fine coverage of the parameter space, and yet is still doable with the available computing power. For each AMOEBA search, we construct the initial simplex with a length scale of 20% of the whole range for each parameter, in hope to have a complete coverage of the whole parameter space. The simulated annealing method is applied in the first 300 model evaluations of an AMOEBA search in order to increase the chances to obtain a “global”  $\chi^2$  minima in the large parameter space to be searched. The AMOEBA search claims a  $\chi^2$  minima if the fractional tolerance `ftol`  $< 10^{-5}$ , and stops if the iteration number exceeds 1000. To find the “true”  $\chi^2$  minima, we restart another AMOEBA search from a claimed  $\chi^2$  minima, but with a  $4\times$  smaller length scale. In the end, two rounds of AMOEBA searches with about eight million model evaluations lead to local  $\chi^2$  minima from  $\chi^2 \sim 52$  to  $\geq 1000$ . As shown in Figure 3, models with black hole masses above  $100/300 M_\odot$  are excluded at the  $\chi_\nu^2 = 3/4$  level. Due to the large photometric fluctuations present in the observations, even the “best” model has  $\chi_\nu^2 > 2$ . Therefore, we do not claim one “true” model for NGC 1313 X-2, but instead consider models with  $\chi^2 < 78$  (i.e.,  $\chi_\nu^2 \leq 3$ ) as “acceptable” models.

The acceptable models are grouped into three categories based on the secondary properties as shown in Figure 4a-e. The secondaries in the first group of models are very young

( $\leq 5$  Myrs) and massive in the carbon core and helium shell burning phase filling about 20% of their Roche lobes. The black hole mass and the inclination angle cluster tightly in small ranges of ( $30\text{-}40M_{\odot}$ ,  $80^{\circ}\text{-}90^{\circ}$ ). The X-ray luminosities are within  $1\text{-}2 \times 10^{40}$  erg/s (about 2-6 times the Eddington luminosity, or  $\sim 2\text{-}6 \times L_E$ ), but the accretion disks are quite small ( $<15\%$  of the tidal-disruption radius) and as thin as the standard thin disk. The accretion disk albedo is in the range of 0-0.5, and the X-ray to thermal conversion factor is above 0.8. The best model in this group (Model A1,  $\chi^2 = 70.88$ ) contains a  $45.3M_{\odot}$  black hole and a young (5 Myrs) and massive (initially  $44M_{\odot}$ , currently  $17M_{\odot}$ ,  $5.1R_{\odot}$ ) secondary that fills 20% of its Roche lobe. As shown in Figure 5a, the optical spectrum is dominated by the hot ( $\sim 70000K$ ) secondary, which is only slightly affected by the X-ray heating. Although the X-ray luminosity is high ( $L_X \sim 1.6 \times 10^{40}$  erg/s  $\sim 3 \times L_E$ ), the optical light from the irradiated accretion disk is only 1% of that from the secondary in the B/V bands because the accretion disk is small ( $X_d \sim 0.05$ ) and thin ( $X_h \sim 1$ ). The binary system is viewed almost edge-on ( $\theta \sim 82^{\circ}$ ), and the predicted sinusoidal light curves have amplitudes of 0.04/0.04 mag in the B/V bands (Figure 5d).

The secondaries in the second group are 40-50 Myrs old in the helium core and hydrogen shell burning phase filling about 40%-80% of their Roche lobes. As compared to the first group, the secondaries are 10 times older and less massive. The black hole mass and the inclination angle occupy much larger parameter ranges of ( $3\text{-}100M_{\odot}$ ,  $20^{\circ}\text{-}80^{\circ}$ ). The X-ray luminosities are  $3 - 30 \times 10^{39}$  erg/s ( $3 - 20 \times L_E$ ), and the accretion disks can be rather large ( $>20\%$  of the tidal-disruption radius) and about 2-6 times thicker than the standard thin disk. The accretion disk albedo and the X-ray to thermal conversion factor on the secondary surface range both from 0.01 to 0.99. The best model in this group (model B1,  $\chi^2 = 54.94$ ) contains a  $15.3M_{\odot}$  black hole and an old (40 Myrs) intermediate-mass (initially  $8.08M_{\odot}$ , currently  $8.07M_{\odot}$ ,  $9.0R_{\odot}$ ) secondary that fills 54% of its Roche lobe. The X-ray luminosity is  $L_X \sim 1.2 \times 10^{40}$  erg/s, or  $\sim 6 \times L_E$ . The secondary has a surface temperature of  $\sim 18500K$  and is significantly affected by the X-ray heating, leading to sinusoidal light curves with amplitudes of 0.15/0.15 mag in the B/V bands for the inclination angle of  $\theta \sim 38^{\circ}$  (Fig 5d). The accretion disk is 55% of the tidal-disruption radius and 3.5 times thicker than the standard thin disk, and the X-ray heated disk contributes roughly equally as the secondary in the B/V bands (Fig 5b).

The secondaries in the third group are 80-160 Myrs old in the helium core and hydrogen shell burning phase filling ( $>98\%$  of) their Roche lobes. As compared to the second group, the secondaries are 2-3 times older and less massive. The black hole mass and the inclination angle cluster tightly in small ranges of ( $3\text{-}10M_{\odot}$ ,  $50^{\circ}\text{-}70^{\circ}$ ). The X-ray luminosities are within  $1 - 2 \times 10^{40}$  erg/s (or  $7 - 20 \times L_E$ ), and the accretion disks can be rather large (40%-70% of the tidal-disruption radius) and about 6-9 times thicker than the standard thin disk. The

accretion disk albedo is constrained within 0.7-0.8, while the X-ray to thermal conversion factor on the secondary surface ranges from 0.01 to 0.8. The best model in this group (model F1,  $\chi^2 = 61.26$ ) contains a  $6.7M_\odot$  black hole and a very old (150 Myrs) and rather low mass (initially  $4.28M_\odot$ , currently  $4.27M_\odot$ ,  $10.6R_\odot$ ) secondary that fills its Roche lobe. The X-ray luminosity is  $L_X \sim 1.9 \times 10^{40}$  erg/s ( $\sim 20 \times L_E$ ), the accretion disk is 40% of the tidal-disruption radius and 7 times thicker than the standard thin disk. The X-ray heated disk contributes about 4 times more light than the secondary in the B/V bands (Fig 5c). The secondary has a surface temperature of  $\sim 9500K$  and is significantly affected by the X-ray heating, leading to sinusoidal light curves with amplitudes of 0.17/0.17 mag in the B/V bands for the inclination angle of  $\theta \sim 56^\circ$  (Fig 5d).

### 3.2. In case of $2K' = 100 \pm 40$ km/s

The model  $\chi^2$  for assumed  $2K' = 100 \pm 40$  km/s is defined in the same way as described in §3.1, and  $\chi^2$  minima are sought in a large phase space with two rounds of AMOEBA searches following the same procedures. The resulted models are grouped into three categories based on the secondary properties as in §3.1, and the “acceptable” models with  $\chi^2 < 78$  are plotted in Figure 6a-f. As compared to the case of  $2K' = 200 \pm 40$  km/s, the first group of models with secondaries in their carbon core and helium shell burning phase are no longer “acceptable”. Even the best model (model A2) for the first group has  $\chi^2 = 84.0$ , an apparently bad fit to the observed light curve as shown in Figure 7.

Models in the second group occupy similar phase space as compared to the case of  $2K' = 200 \pm 40$  km/s, while the best model is quite different. As shown in Figure 6-7, the best model (model B2,  $\chi^2 = 51.9$ ) contains a  $39M_\odot$  black hole and a 50Myrs old intermediate mass secondary (initially  $7.18M_\odot$ , currently  $7.16M_\odot$ ,  $8.2R_\odot$ ) in its helium core and hydrogen shell burning phase filling 51% of its Roche lobe. The X-ray luminosity is  $L_X \sim 1.2 \times 10^{40}$  erg/s, or  $\sim 2.4 \times L_E$ . The accretion disk is 15% of the tidal-disruption radius and 5 times thicker than the standard thin disk, and the X-ray heated disk contributes two times that of the secondary in the B/V bands. The secondary has a surface temperature of  $\sim 17500K$  and is significantly affected by the X-ray heating, leading to sinusoidal light curves with amplitudes of 0.155/0.155 mag in the B/V bands for the inclination angle of  $\theta \sim 45^\circ$  (Fig 7).

Models in the third group occupy roughly similar phase space as compared to the case of  $2K' = 200 \pm 40$  km/s, while the secondaries are older and less massive. The best model (model F2,  $\chi^2 = 55.8$ ) contains a  $8.2M_\odot$  black hole and a 200 Myrs old secondary (initially  $3.75M_\odot$ , currently  $3.74M_\odot$ ,  $9.9R_\odot$ ) in its helium core and hydrogen shell burning phase filling its Roche lobe. The X-ray luminosity is  $L_X \sim 9 \times 10^{39}$  erg/s ( $\sim 8.5 \times L_E$ ), the accretion disk

is 30% of the tidal-disruption radius and 6 times thicker than the standard thin disk. The X-ray heated disk contributes about 4 times that of the secondary in the B/V bands. The secondary has a surface temperature of  $\sim 8700K$  and is significantly affected by the X-ray heating, leading to sinusoidal light curves with amplitudes of 0.156/0.156 mag in the B/V bands for the inclination angle of  $\theta \sim 38^\circ$  (Fig 7).

### 3.3. In case of $2K' = 25 \pm 15$ km/s

The model  $\chi^2$  for assumed  $2K' = 25 \pm 15$  km/s is defined in the same way as described in §3.1, and  $\chi^2$  minima are sought in a large phase space with two rounds of AMOEBA searches following the same procedures. The resulted models are grouped into three categories based on the secondary properties as in §3.1, and the “acceptable” models with  $\chi^2 < 78$  are plotted in Figure 8a-f. As compared to the case of  $2K' = 200 \pm 40$  km/s, the first group of models with secondaries in their carbon core and helium shell burning phase are no longer “acceptable” like the case of  $2K' = 100 \pm 40$  km/s. Even the best model (model A3) for the first group has  $\chi^2 = 96.5$ , an apparently bad fit to the observed light curve as shown in Figure 9.

Models in the second group occupy similar phase space as compared to the case of  $2K' = 200 \pm 40$  km/s, except that the black hole mass can be above  $1000M_\odot$ . The best model (model B3,  $\chi^2 = 52.43$ ) contains a  $275M_\odot$  black hole and a 40Myrs old intermediate mass secondary (initially  $8.09M_\odot$ , currently  $8.08M_\odot$ ,  $7.9R_\odot$ ) in its helium core and hydrogen shell burning phase filling 44% of its Roche lobe. The X-ray luminosity is  $L_X \sim 1.3 \times 10^{40}$  erg/s, or  $\sim 0.4 \times L_E$ . The accretion disk is 12% of the tidal-disruption radius and 4 times thicker than the standard thin disk, and the X-ray heated disk contributes 1.7 times that of the secondary in the B/V bands. The secondary has a surface temperature of  $\sim 20000K$  and is significantly affected by the X-ray heating, leading to sinusoidal light curves with amplitudes of 0.157/0.157 mag in the B/V bands for the inclination angle of  $\theta \sim 73^\circ$  (Fig 9).

Models in the third group occupy roughly similar phase space as compared to the case of  $2K' = 200 \pm 40$  km/s, while the secondaries are older and less massive. The best model (model F3,  $\chi^2 = 53.89$ ) contains a  $6.1M_\odot$  black hole and a 220 Myrs old secondary (initially  $3.58M_\odot$ , currently  $3.57M_\odot$ ,  $9.8R_\odot$ ) in its helium core and hydrogen shell burning phase filling its Roche lobe. The X-ray luminosity is  $L_X \sim 1.6 \times 10^{40}$  erg/s ( $\sim 20 \times L_E$ ). The secondary has a surface temperature of  $\sim 8200K$  and is significantly affected by the X-ray heating, leading to sinusoidal light curves with amplitudes of 0.156/0.156 mag in the B/V bands for the inclination angle of  $\theta \sim 15^\circ$  (Fig 9). The accretion disk is 28% of the tidal-disruption radius and 6 times thicker than the standard thin disk, and the X-ray heated disk contributes

about 2 times that of the secondary in the B/V bands.

The best models for the three cases are listed in Table 1. To summarize, there are three groups of acceptable models based on the secondary properties depending on whether the secondary is in the carbon core and helium shell burning phase or in the helium core and hydrogen shell burning phase, and whether the secondary is filling the Roche lobe or just part of the Roche lobe. The first group of models with secondaries in the carbon core and helium shell burning phase, while acceptable for the highest  $2K' = 200 \pm 40$  km/s, become unacceptable when  $2K'$  drops. Models of the other two groups, with secondaries in the helium core and hydrogen shell burning phase, are acceptable for all cases of assumed  $2K'$ , but the black hole mass can become as massive as  $1000M_{\odot}$  as the assumed  $2K'$  becomes lower as shown in Figure 10. We note that, while the extinction value is started to range from 0.11 mag to 0.44 mag, it is always close to  $E(B-V)=0.11$  mag for all three groups of “acceptable” models regardless the assumed  $2K'$  as shown in Figure 4f/6f/8f.

#### 4. DISCUSSION

In this work, we constrain the binary masses and other parameters for ULX NGC 1313 X-2 by fitting observations to an X-ray irradiated binary model. The model is based on the eclipsing binary light curve code by Jerome Orosz (Orosz & Hauschildt 2000; Orosz et al. 2007) with accommodations for the X-ray irradiation of the accretion disk and the secondary in the ULX systems. This model treats the accretion disk as a standard disk that can be fattened due to X-ray irradiation. The disk fattening factor should be linked to the X-ray luminosity; however, the exact relation is not well studied, and for now these two parameters are allowed to vary independently in our model. The X-ray heating of the disk and the secondary surface is treated the same way as in the cases of Galactic X-ray binaries (Vrtilek et al. 1990; FKR2002; Copperwheat et al. 2005) with two parameters, disk albedo  $\beta$  and the X-ray-to-thermal conversion factor  $\gamma$ , respectively. While  $\beta$  and  $\gamma$  can be calculated given the disk/secondary surface structure and incident flux, such calculations are beyond the scope of this work, and we simply allow them to vary between 0 and 1 exclusive. The model describes the (X-ray heated) secondary surface with Kurucz stellar atmosphere model, allowing to calculate the emergent spectrum with absorption lines from the secondary.

NGC 1313 X-2 is chosen for this study because it is so far the only ULX with the orbital period, B/V light curves and the black hole’s radial velocity amplitude. Our HST GO program has obtained the B/V light curves and an orbital period of  $P = 6.12 \pm 0.16$  days for NGC 1313 X-2 (Liu et al. 2009), while the black hole’s radial velocity amplitude is measured from the disk emission line HeII  $\lambda 4686\text{\AA}$  (Pakull et al. 2006; Roberts et al.

2010; Gladstone et al. 2011). The observed HeII  $\lambda 4686\text{\AA}$  shift may deviate from the true amplitude for the black hole (e.g., due to the emission line genesis location change under different X-ray luminosities), as implied by the phase shift between the radial velocity curve and the light curve often seen in Galactic accreting binaries. Indeed, a comprehensive study shows that the semi-amplitude measured with disk emission lines can differ from the true value by a factor of 0.9~2.5 (Cantrell & Bailyn 2007). The black hole mass measurements based on the disk emission lines are thus considered less reliable as compared to those based on absorption/emission lines from the secondary, and not commonly used for Galactic black hole binaries given the detectability of absorption or Bowen fluorescent lines from their secondaries. For most ULXs with their faint optical counterparts, however, the disk emission line method is the only way to estimate the black hole masses, with an accuracy that is not superb but enough to determine whether they are stellar mass black holes or IMBHs.

Dynamical models for NGC 1313 X-2 are sought with the Monte Carlo sampling of the parameter space followed by two rounds of AMOEBA searches of  $\chi^2$  minima. Given that the observed He II  $\lambda 4686\text{\AA}$  emission line shift ( $\sim 180 \pm 40$  km/s) can be 0.9-2.5 times that of the true radial velocity amplitude of the black hole, the true amplitude can be  $\sim 200$ -70 km/s. We thus have tested cases of  $2K' = 200 \pm 40$  km/s and  $2K' = 100 \pm 40$  km/s, and additional case of  $2K' = 25 \pm 15$  km/s. While the model parameters are allowed to vary in ranges as large as possible to not miss any acceptable models, the available observations are able to exclude most of the parameter space. For example, the extinction value is found to be  $E(B-V) = 0.11$  mag for all acceptable models with  $\chi_\nu^2 < 3$  regardless the assumed  $2K'$  values, although it is allowed to vary between 0.11 and 0.44 mag. Interestingly, independent measurements with nebular lines showed that  $E(B-V) = 0.11$  mag (Pakull et al. 2006), justifying our model fits. When X-ray irradiation parameters  $\beta$ ,  $\gamma$  and the dependency of the disk thickness on the X-ray luminosity are further constrained by physical considerations, some acceptable models may become unacceptable. However, no unacceptable models can become acceptable given such additional constraints.

While  $\chi_\nu^2 \sim 1$  for the true model is expected when there are only Poisson errors for the photometric measurements, all models obtained from the fitting have  $\chi_\nu^2 > 2$ . This is because the HST light curves of NGC 1313 X-2 are afflicted with photometric fluctuations caused by, e.g., X-ray variations between observations. Such photometric fluctuations are clearly present as shown in Figure 5d, even after we exclude five F555W observations with abnormally red colors that exhibit extremely large deviations from the fitted sinusoidal light curve. We thus do not claim one “true” model, but instead consider models with  $\chi_\nu^2 < 3$  as “acceptable” models, which fall into three groups based on the secondary properties. The first group of models have 4-5 Myrs old secondaries in the carbon core and helium shell burning phase filling only 20% of its Roche lobe, the second group of models have 40-50

Myrs old secondaries in the helium core and hydrogen shell burning phase filling 40%-80% of its Roche lobe, while the third group have 150-220 Myrs old secondaries in the helium core and hydrogen shell burning phase filling its Roche lobe.

The acceptable models can be further assessed with additional constraints. The first group of models have X-ray luminosities of  $1-2 \times 10^{40}$  erg/s, or 2-6 times the Eddington luminosity, yet the accretion disks are as thin as the standard thin disk. This contradicts the understanding that a standard disk forms under a few tenths of the Eddington luminosity based on observations of Galactic black hole X-ray binaries (Remillard & McClintock 2006). ESO/VLT and SUBARU studies show that the stellar environment around NGC 1313 X-2 is about 40-70 Myrs old (Pakull et al. 2006). This is quite consistent with the secondary age of 40-50 Myrs for the second group, but significantly different from the secondary age of 150-220 Myrs for the third group and the secondary age of 4-5 Myrs for the first group. Thus, the second group of models are the only possible models given the dynamical constraints, the reasonableness of the accretion disk, and the observed stellar environment age.

Concerns arise whether the secondaries in the second group can provide the required accretion rate to power the observed X-ray luminosity. Unlike the third group where secondaries are filling the Roche lobe, the black holes in the second group must accrete via capturing the focused stellar winds from the secondaries that are only filling 40%-80% of the Roche lobe. The stellar wind mass loss rate for these secondaries is usually around  $10^{-8} M_{\odot}/\text{yr}$  based on the de Jager et al. (1988) prescription, but the observed average X-ray luminosity of  $4 \times 10^{39}$  erg/s requires an accretion rate of  $\dot{M} \sim 8 \times 10^{-7} M_{\odot}/\text{yr}$  regardless the black hole mass. However, the de Jager et al. prescription describes stars in isolation, while the secondaries in the second group are in a close binary configuration, where the equivalent surface gravity is reduced by the gravitational pull exerted by the companion black hole. Numerical calculations have shown that the mass loss rate due to this reduced surface gravity can be boosted by more than an order of magnitude if the secondary is almost filling its Roche lobe (Frankowski & Tytenda 2001). In addition, the strong X-ray radiation from the accretion disk will heat up the secondary surface and increase the kinetic energy of the surface materials, and possibly enhance the mass loss further.

The black hole mass for NGC 1313 X-2 ranges from a few to above  $1000 M_{\odot}$  depending on the true radial velocity amplitude of the black hole. Figure 10 shows the black hole mass versus the black hole radial velocity semi-amplitude for all acceptable models from this work, with larger symbols for more likely models of lower  $\chi^2$  values. The black hole mass can be 3-10  $M_{\odot}$  (e.g., model B1) if  $K' = 120-140$  km/s, or 20-30  $M_{\odot}$  if  $K' = 65-75$  km/s, or 30-50  $M_{\odot}$  (e.g., model B2) if  $K' = 40-60$  km/s. If the true radial velocity semi-amplitude is lower than 40 km/s, the black hole mass can be a few  $M_{\odot}$  (e.g., model B3b as listed in

Table 1), a few  $\times 10M_{\odot}$ , a few  $\times 100M_{\odot}$  (e.g., model B3), or above  $1000 M_{\odot}$ . While the death of stars with solar metallicity can not produce black holes more massive than  $10M_{\odot}$  (Fryer & Kalogera, 2001), NGC 1313 X-2 is located in an environment of  $0.1-0.2Z_{\odot}$  (Ryder 1993), and a black hole up to  $50M_{\odot}$  may be produced. Indeed, massive black holes have been discovered in environments of similarly low metallicities, e.g., the black hole of  $\sim 16M_{\odot}$  for M33 X-7 (Orosz et al. 2007), and the black hole of  $23-35 M_{\odot}$  for IC 10 X-1 (Silverman & Filippenko 2009). Therefore, NGC 1313 X-2 can be a black hole of up to a few  $\times 10M_{\odot}$  that may be explained by the stellar evolution of low metallicity stars, or an IMBH of a few  $\times 100M_{\odot}$  or above  $1000M_{\odot}$  if the true black hole radial velocity semi-amplitude is more than 5 times lower than the observed velocity shift. Such IMBHs can not be produced through the death of stars, but may form in the centers of dense stellar clusters via the merging of stellar mass black holes (e.g., Miller & Hamilton 2002), or from the direct collapse of merged supermassive stars in very dense star clusters (e.g., Portegies Zwart & McMillan 2002).

Further observations are required to determine whether NGC 1313 X-2 is a massive stellar black hole or an IMBH. Current observations use the HeII  $\lambda 4686\text{\AA}$  disk emission line to constrain the radial motion of the black hole, which is difficult due to the weakness of the line, the line genesis location change and the contamination from the surrounding nebula. Such complications can be circumvented if UV emission lines are used to measure the radial velocity shift, because the UV emission lines are usually two orders of magnitudes more luminous than the HeII  $\lambda 4686\text{\AA}$  line. For example, X-ray illuminated disk and corona model predicts that the line luminosities for N V  $\lambda 1240\text{\AA}$ , Si IV  $\lambda 1396\text{\AA}$ , and C IV  $\lambda 1550\text{\AA}$  are 390, 186, 373 times that of HeII  $\lambda 4686\text{\AA}$ , quite consistent with observations of several X-ray binaries (Raymond 1993). The model also shows that the HeII  $\lambda 4686\text{\AA}$  line is produced mostly in the inner disk region, a small region that is easily affected by small changes in the accretion rate or X-ray luminosity, resulting in line genesis location changes and apparent line centroid changes. In contrast, the above UV emission lines are produced across the whole disk, and are less affected by small changes in the accretion rate or X-ray luminosities. This reduces the line centroid changes due to X-ray luminosity changes as compared to the HeII  $\lambda 4686\text{\AA}$  line. In addition, these UV emission lines cannot form in the surrounding nebula, thus are free of nebular contamination. Observations of these UV emission lines can be carried out with Cosmic Origin Spectrograph (COS) aboard Hubble Space Telescope.

Better light curves are also required to determine whether NGC 1313 X-2 is a massive stellar black hole or an IMBH. Given the better determined radial motion of the black hole, the black hole mass can still range from a few to a few  $\times 10M_{\odot}$  to a few  $\times 100M_{\odot}$  to above  $1000M_{\odot}$ . Although all models have similar light curves in the HST F450W/F555W bands as resulted from the  $\chi^2$  minimization process, the predicted light curves can be quite different in other bands given the difference in the secondaries, the inclination angles and the X-ray

heating effects. As shown in Figure 11 as examples, the predicted light curves of model B3 and B3b for  $K' \sim 20$  km/s, while similar in WFPC2 F450W/F555W bands, are offset by 0.04 in the WFC3/UVIS F275W band and by 0.02 mag in the WFC3/UVIS F814W band. Such difference can be easily detectable with HST with reasonable exposure time, and can be used to distinguish between a stellar black hole (model B3b) and an IMBH (model B3). Because the X-ray heating of the accretion disk and the secondary surface are important in these models, the photometric monitoring observations should be accompanied by quasi-simultaneous X-ray observations with, e.g., swift/XRT, in order to assess the X-ray heating effects of the light curves.

We would like to thank Dr. Jeffery E. McClintock and Rosanne Di Stefano for helpful discussions. The computations in this paper were run on the Odyssey cluster supported by the FAS Science Division Research Computing Group at Harvard University.

## REFERENCES

- Begelman, M.C., 2002, ApJ, 568, L97
- Cantrell, A. & Bailyn, C., 2007, ApJ, 670, 727
- Colbert, E. J. M. and Mushotzky, R. F. 1999, ApJ, 519, 89
- Copperwheat, C., Cropper, M., Soria, R., Wu, K., 2005, MNRAS, 362, 79
- de Jager, C., Nieuwenhuijzen, H., van der Hucht, K. A. 1988, A&AS, 72, 259
- Fabbiano, G. 1989, ARA&A, 27, 87
- Feng, H. and Kaaret, P., 2006, ApJ, 650, 75L
- Frankowski, A. & Tylenda, R., 2001, A&A, 367, 513
- Frank, J., King, A., and Raine, D, 2002, *Accretion Power in Astrophysics*, §5.10
- Fryer, C. L. & Kalogera, V., 2001, ApJ, 554, 548-560
- Georganopoulos, M., Aharonian, F.A., and Kirk, J.G., 2002, A&A, 388, L25
- Girardi, L., Bertelli, G., Bressan, A., et al. 2002, A&A, 391, 195.
- Gladstone, J. C., Roberts, T. P., Done, C. 2009. MNRAS, 397, 1836

- Gladstone, J. C., Roberts, T. P., et al. 2011, in preparation
- Gri , F., Pakull, M. W., Soria, R., et al. 2008, *A&A*, 486, 151
- Guti rrez, C.M., 2006, *ApJ*, 640, 17L
- Haines, E., 1994, *Graphics Gems IV*, p. 24-46
- Kaaret, P. & Corbel, S. 2009, *ApJ*, 697, 950
- King, A. R., Davies, M. B., Ward, M. J., Fabbiano, G. and Elvis, M. 2001, *ApJ*, 552, L109
- Kopal, Z., *Close Binary Systems*, 1959, p136
- Kurucz, R.L., 1993, Kurucz CD-ROM No. 13. Stellar Atmosphere Programs and 2 km/s Grid
- Liu, J. 2009, *ApJ*, 704, 1628
- Liu, J., Bregman, J., and Seitzer, P., 2002, *ApJL*, 580, 31
- Liu, J., Bregman, J., and Seitzer, P., 2004, *ApJ*, 602, 249
- Liu J., Bregman J., & McClintock, J., 2009, *ApJL*, 679, 37
- Liu, J.; Bregman, J.; Miller, J. & Kaaret, P., 2007, *ApJ*, 661, 165
- Liu, J. & Di Stefano, R. 2008, *ApJL*, 674, 73
- Lucy, L. B., 1967, *ZA*, 65, 89
- Miller, M. & Hamilton, D., 2002, *MNRAS*, 330, 232
- Mucciarelli, P., Zampieri, L., et al. 2005, *ApJ*, 633, L101
- Orosz, J.A. & Hauschildt, P.H., 2000, *A&A*, 364, 265
- Orosz, J.A., McClintock, J.E., et al. 2007, *Nature*, 449, 872
- Pakull, M.W., Grise, F., and Motch, C., 2006, *IAUS*, 230, 293 (astro-ph/0603771)
- Portegies Zwart, S., and McMillan, S., 2002, *ApJ*, 576, 899
- Press, W., Flannery, B., Teukolsky, S., Vetterling, W., 2003, *Numerical Recipe in C*, Cambridge University Press
- Ramsey, C., Williams, R., et al. 2006, *ApJ*, 641, 241

- Raymond, J. 1993, ApJ, 412, 267
- Roberts, T. P., Gladstone, J.C., Goulding, A.D., et al. 2010, to be published in *Astronomische Nachrichten* (astro-ph/1011.2155)
- Roberts, T.P.; Levan, A. J.; Goad, M. R. 2008, MNRAS, 387, 73
- Ryder, S. D. 1993, Ph.D. thesis, Australian National Univ.
- Shakura, N., and Sunyaev, R., 1973, A&A, 24, 337
- Strohmayer, T., and Mushotzky, R., 2003, ApJL, 586, 61L
- Tully R.B, 1988, *Nearby Galaxies Catalogue*, Cambridge University Press.
- van Paradijs, J., and McClintock, J., 1994, A&A, 290, 133
- von Zeipel H., 1924, MNRAS, 84, 702
- Vrtilek, S.D., Raymond, J.C., Garcia, M.R. et al. 1990, A&A, 235, 162
- Zampieri, L., Mucciarelli, P. et al., 2004, ApJ, 603, 523
- Zampieri, L., Impiombato, D., Falomo, R. et al., 2011, MNRAS, in press

## A. A Brief Model Description

To fully model the X-ray irradiated binaries like ULXs, one needs to consider the gravitational distortion of the secondary, the accretion disk, and the X-ray irradiation effects. Below we describe our treatments of these problems, and how we calculate the emergent spectra and light curves, followed by examples of model outputs to illustrate the model dependence on key parameters.

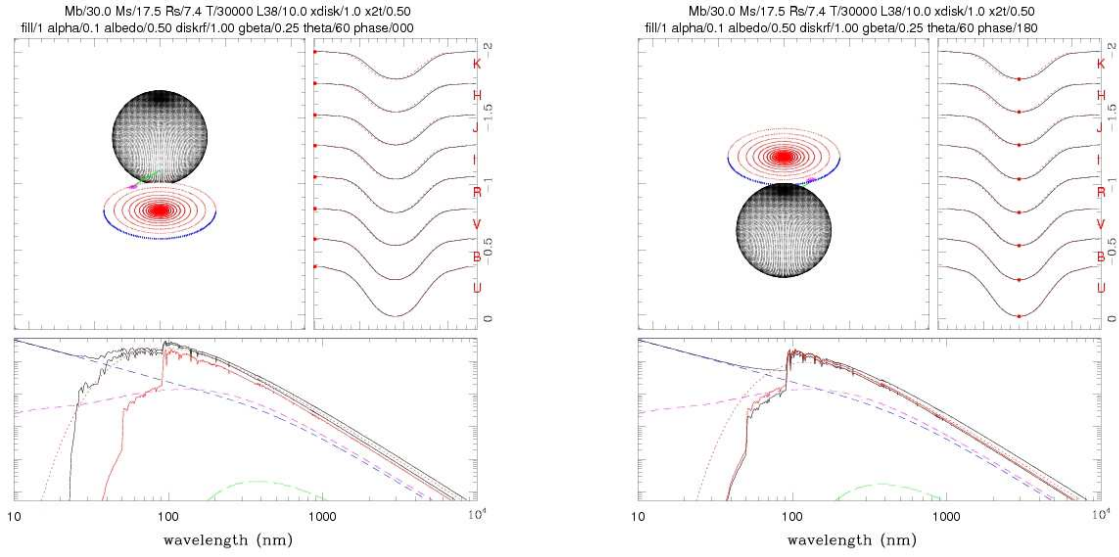


Fig. 1.— Model output for (a) phase 0 and (b) phase 180 for the base model with  $M_{\bullet} = 30M_{\odot}$ , a B0V secondary ( $M_{*} = 17.5M_{\odot}$ ,  $R_{*} = 7.4R_{\odot}$ , and  $T_{*} = 30,000$  K with solar abundance),  $L_X = 10^{39}$  erg s $^{-1}$ ,  $X_h = 1$ ,  $X_d = 0.5$ ,  $\beta = 0.5$ ,  $\gamma = 0.5$ , and  $\Theta = 60^{\circ}$ . In each figure, the upper left panel shows the binary components projected on the plane normal to  $\hat{v}$ , and the upper right panel shows the  $UBVRIJHK$  light curves for a whole period with the magnitudes marked for this phase. The lower panel shows the emergent spectra from the secondary with (black solid) and without (red solid) X-ray irradiation, from the disk itself (blue long-dash) and the X-ray irradiation contribution (purple long-dash), and from the binary as a whole (the uppermost black solid). The red dotted is the blackbody approximation of the heated star spectrum. The wavelength unit is nanometer (nm).

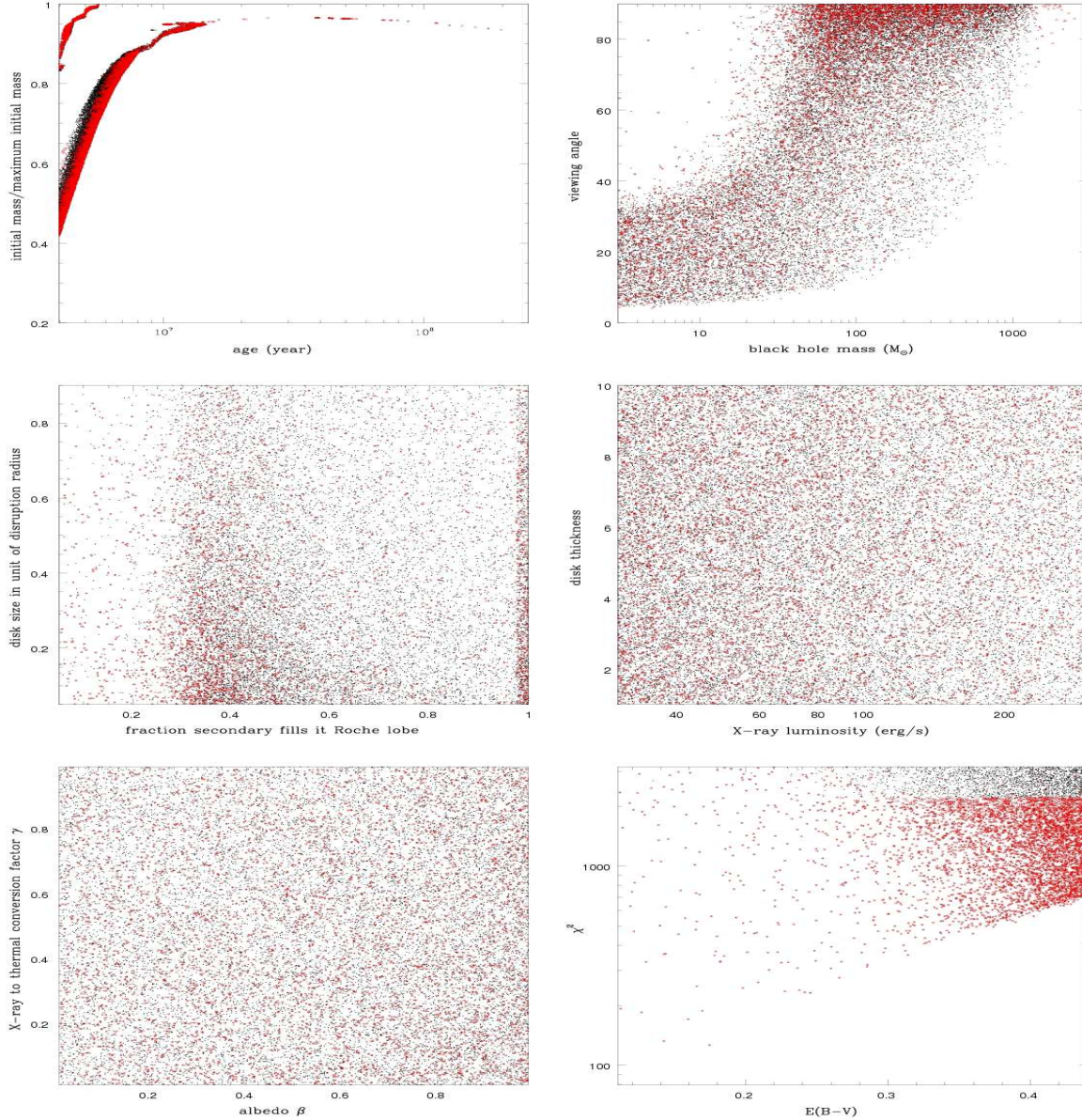


Fig. 2.— Models with  $\chi^2 < 10000$  (black dots) for assumed  $2K' = 200 \pm 40$  km/s. The six panels show (a) the secondary age vs initial mass, (b) the black hole mass vs inclination angle, (c) the fraction the secondary fills its Roche lobe vs the disk size in unit of disruption radius, (d) the X-ray luminosity vs the disk thickness, (e) the disk surface albedo vs the X-ray-to-thermal conversion factor on the secondary surface, and (f) the extinction  $E(B-V)$  vs the model  $\chi^2$ . The red dots show the models selected as starting points for AMOEBA searches. Note that the considerations in the accretion rate lead to the concentration of models with secondaries filling ( $>98\%$  of) the Roche lobe in (c).

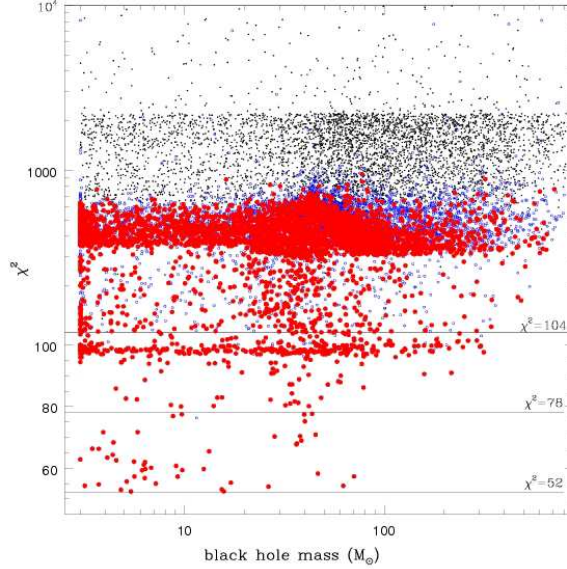


Fig. 3.— The black hole mass versus  $\chi^2$  for models selected from the monte carlo sampling of the phase space as starting points for AMOEBA searches (black thin dots), the results for the first round of AMOEBA searches (blue open circles) and for the second round of AMOEBA searches (red filled circles). The horizontal lines denote  $\chi^2=52/78/104$  (i.e.,  $\chi_\nu^2=2/3/4$ ).

### A.1. Roche geometry

We follow the formulation of Kopal (1959) to compute the Roche lobe for given  $M_\bullet$ ,  $M_*$ , and  $a$  (i.e., primary and secondary masses and separation). In our computation, we define a Cartesian coordinate system with  $a$  as the unit length to place the secondary at  $(0, 0, 0)$  and the primary at  $(1, 0, 0)$ . The Roche potential at each point  $(x, y, z)$  is

$$\Phi(x, y, z) = -GM_*/r_1 - GM_\bullet/r_2 - G(M_\bullet + M_*)r^2/2$$

where  $r_1 = \sqrt{x^2 + y^2 + z^2}$ ,  $r_2 = \sqrt{(x - 1)^2 + y^2 + z^2}$  and  $r^2 = (x - M_\bullet/(M_\bullet + M_*))^2 + y^2$ . The L1 point is located at  $(x_1, 0, 0)$ , with  $x_1$  solved numerically from  $x_1^{-1} - x_1 = M_\bullet/M_*[(1 - x_1)^{-2} - (1 - x_1)]$ . To compute the Roche lobe, we set up a polar coordinate system  $(r, \theta, \phi)$ , and solve numerically for each of the  $\theta, \phi$  grid the radius  $r$  at which the Roche potential is the same as at the L1 point. The effective radius  $R_{L,*}$  (in unit of  $a$ ) for the Roche lobe around the secondary is computed from the volume ( $V = 4\pi R_{L,*}^3/3$ ) enclosed by the equipotential surface. The effective radius  $R_{L,\bullet}$  is also computed for the Roche lobe around the primary black hole.

A secondary with mass  $M_*$ , radius  $R_*$ , surface temperature  $T_*$  and gravity  $g_*$  ( $= GM_*/R_*^2$ ) is filled into its Roche lobe by equating  $a \cdot R_{L,*} f_R = R_*$ , with  $f_R$  as the frac-

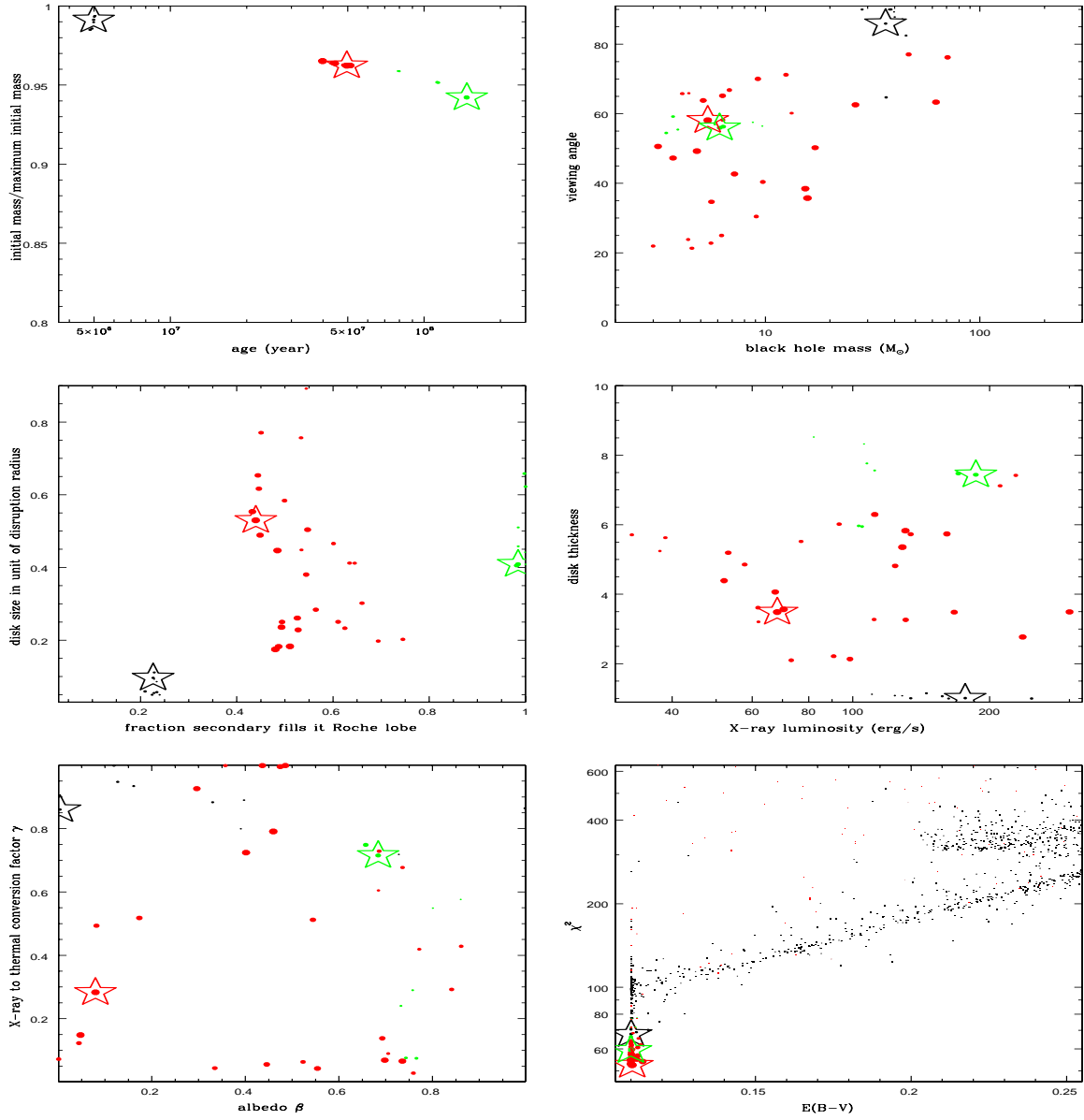


Fig. 4.— Models with  $\chi^2 < 78$  obtained with two rounds of AMOEBA searches. Models are divided into groups one (black), two (red) and three (green). The symbol sizes are inversely scaled with the  $\chi^2$  values of the models. The three asterisks are model A1 (black), model B1 (red) and model F1 (green) as described in the text. The six panels show (a) the secondary age vs initial mass, (b) the black hole mass vs inclination angle, (c) the fraction the secondary fills its Roche lobe vs the disk size in unit of disruption radius, (d) the X-ray luminosity vs the disk thickness, (e) the disk surface albedo vs the X-ray-to-thermal conversion factor on the secondary surface, and (f) the extinction  $E(B-V)$  vs the model  $\chi^2$  for models with  $\chi^2 < 600$ .

tion the secondary fills its Roche lobe. This immediately sets the physical dimension for  $a$  and the orbital period with

$$P^2 = 2\pi a^3 / G(M_\bullet + M_*)$$

The gravity at each surface element of the Roche lobe can be computed as

$$\vec{g} \equiv g\hat{g} = \nabla\Phi(x, y, z) = (\partial/\partial x, \partial/\partial y, \partial/\partial z)\Phi(x, y, z)$$

and  $-\hat{g}$  is the surface normal vector. This gravity varies over the stellar surface. It is higher near the poles and lower near the equators, and the lowest at the parts of the star nearest to the L1 point. In hydrostatic equilibrium, the gravity variation modifies the local effective temperature over the stellar surface. To describe this gravitational darkening (brightening) effect, we adopt the scaling relation  $T_g = T_*(g/g_*)^b$  with  $b=1/4$  for radiative stellar atmospheres (von Zeipel, 1924) and  $b=0.08$  for convective atmospheres (Lucy, 1967).

## A.2. Accretion disk

The accretion disk around the black hole is described as a standard accretion disk with the  $\gamma$  prescription (Shakura & Sunyaev 1973; Frank, King & Raine 2002, hereafter FKR2002). For such an accretion disk with radius  $r$ , the inner radius  $r_i = 6GM_\bullet/c^2$  assuming a non-spinning black hole, the luminosity  $L_d = GM_\bullet\dot{M}_\bullet/2r_i$ , and the temperature profile  $T_a(r) = T_0(r_i/r)^{3/4}f$  with  $f^4 = 1 - (r_i/r)^{1/2}$  and  $T_0^4 = 3L_d/4\pi\sigma r_i^2$ . To avoid tidal disruption, the disk must be within the tidal radius  $R_{Tides} \approx 0.9R_{L,\bullet}$ . We assume the outer radius  $r_o = X_r \cdot R_{Tides}$  with  $X_r \leq 1$ . The disk can be divided into the inner disk, the middle disk, and the outer disk, with the transitions at  $r_{im} = 3.6 \times 10^2 \gamma^{2/21} \dot{m}^{16/21} m^{2/21} f^{64/21}$  and at  $r_{mo} = 2.6 \times 10^4 \dot{m}^{2/3} f^{8/3}$ . Here  $m = M_\bullet/M_\odot$ ,  $\dot{m} = \dot{M}_\bullet/\dot{M}_{Edd}$ ,  $\dot{M}_{Edd} = L_{Edd}/0.1c^2$ , and  $L_{Edd} = 4\pi GM_\bullet c/\kappa = 1.3 \times 10^{38} m \text{ erg s}^{-1}$ . The height of the disk  $h(r) = 7.5\dot{m}f^4$  for the inner disk,  $h(r) = 1.6 \times 10^{-2} \gamma^{-1/10} \dot{m}^{1/5} m^{-1/10} r^{21/20} f^{4/5}$  for the middle disk, and  $h(r) = 7.2 \times 10^{-3} \gamma^{-7/10} \dot{m}^{3/20} m^{-1/10} r^{9/8} f^{3/5}$  for the outer disk. In our model, we assume the “real” disk height  $H(r) = X_h \cdot h(r)$  to account for the fattened disk at high X-ray luminosities. With the above formulae, we compute the surface temperature  $T(r)$ , height  $H(r)$  and surface normal vector  $\hat{s}(\vec{r})$  for the disk under the reasonable assumption that  $L_X = L_d$ , i.e., X-ray dominates the disk radiation in ULXs.

### A.3. X-ray irradiation

X-ray irradiation of the accretion disk is treated following FKR2002 (§5.10). The X-ray flux crossing the disk surface at  $\vec{r}$  is

$$F = \frac{L_X}{4\pi d^2} (1 - \beta) \cos \psi$$

with  $\vec{d} = d\hat{d} = \hat{d}\sqrt{r^2 + H^2(r)}$  as the vector from the black hole to the surface element,  $\beta$  as the albedo, and  $\cos \psi = -\hat{s} \cdot \hat{d}$  representing the angle between the direction of the incident radiation and the disk surface normal vector. The effective temperature resulting from irradiation can be defined as

$$T_{Irr}^4 = F/\sigma = \frac{1}{3} T_0^4 (r_i/d)^2 (1 - \beta) \cos \psi$$

and the total temperature for the disk surface element

$$T_d^4 = T_a^4(r) + T_{Irr}^4$$

The X-ray irradiation of the secondary is treated in a similar fashion. With respect to the black hole, a stellar surface element at  $(x, y, z)$  raises above the orbital plane with an angle of  $\delta = \arcsin \frac{z}{d}$  to the black hole with  $\vec{d} = d\hat{d} = (x - 1, y, z)$ , while the accretion disk edge at the outer radius  $r_o$  raises above the orbital plane with an angle of  $\Delta = \arctan \frac{H(r_o)}{r_o}$ . The effective temperature from irradiation is defined as

$$T_{Irr,*}^4 = \frac{1}{3} Q T_0^4 (r_i/d)^2 \gamma \cos \psi$$

with  $\cos \psi = -\hat{d} \cdot \hat{g}$ ,  $\hat{g}$  as the surface normal vector,  $Q$  as the transmission function, and  $\gamma$  representing the fraction of intercepted X-ray flux converted to thermal energy. The stellar surface element with  $\cos \psi < 0$  is blocked by the star itself and thus not irradiated. The transmission function describes how the X-ray is blocked by the accretion disk, with  $Q = 0$  if  $\delta < \Delta$  (i.e., completely blocked), and  $Q = 1 - e^{-\frac{\delta - \Delta}{\Delta}}$  if  $\delta > \Delta$  to account for the photoelectric absorption by the extended disk atmosphere. The total temperature at each element of the secondary surface is then computed as

$$T_s^4 = T_g^4 + T_{Irr,*}^4$$

### A.4. Viewing the binary

Whether a surface element of the accretion disk or the secondary is visible to the observer at an inclination of  $\Theta$  is determined as follows. For each binary phase  $\Phi$  with the observing

vector  $\hat{v}(\Theta, \Phi)$  from the binary to the observer, treated first is the component closer to the observer, which is the accretion disk at  $-\frac{\pi}{2} < \Phi < \frac{\pi}{2}$  and the secondary at  $\frac{\pi}{2} < \Phi < \frac{3\pi}{2}$  under the convention that  $\Phi = 0$  if the accretion disk is right in between the secondary and the observer. For the accretion disk, the disk surface may for some  $\Theta$  be blocked by the disk edge, which is treated as a cylinder with a radius of  $r_o$ , a half height of  $H(r_o)$ , a surface temperature of  $T_a(r_o)$ , and a surface normal vector  $\hat{m}$ . We thus project the visible parts of the disk edge (with  $\hat{m} \cdot \hat{v} \geq 0$ ) onto a plane normal to  $\hat{v}$ , and compute its silhouette as a polygon. For the disk surface elements, visible are those with  $\hat{s} \cdot \hat{v} \geq 0$  and outside the edge's silhouette. A disk silhouette is computed for the disk edge and surface as a whole. For the secondary, we examine the surface elements from pole to pole, and compute a silhouette polygon of all previously examined elements for each latitude. A secondary surface element is visible if it is outside the previous silhouette polygon and with  $-\hat{g} \cdot \hat{v} \geq 0$ . We then treat the component farther away from the observer in the same way, except that a surface element is invisible if it is within the silhouette polygon for the closer component. The ray-tracing method developed by Haines (1994) is used to check whether a surface element, after projecting to the plane normal to  $\hat{v}$ , is within a silhouette polygon.

### A.5. Model output

Both the spectrum and the wide-band photometry are computed for the emergent emission from the X-ray irradiated binary model. For the  $i$ -th visible surface element, the flux is computed as

$$\Delta F_i(\lambda) = I_i(\lambda) \frac{A_i \cos \Psi_i}{D^2}$$

with  $I_i(\lambda)$  as the specific intensity,  $A_i \cos \Psi_i$  as the surface element area projected along the line of sight, and  $D$  as the distance to the observer. Here  $\cos \Psi = \hat{v} \cdot -\hat{g}$  for the secondary,  $\cos \Psi = \hat{v} \cdot \hat{s}$  for the disk surface, and  $\cos \Psi = \hat{v} \cdot \hat{m}$  for the disk edge. The disk edge and surface are treated simply as a black body, and  $I_i(\lambda) = B_\lambda(T_d)$ . The secondary is treated as Kurucz's stellar atmosphere model (Kurucz 1993), which gives the emergent intensity spectrum  $I(\lambda; \mu, T, g)$  for a grid of the incident angle  $\mu$ , surface temperature  $T$  and gravity  $g$  (ref). In our model, the intensity spectrum  $I_i(\lambda) = I(\lambda; \mu_i, T_{s,i}, g_i)$  is interpolated from the model grid with  $\mu = \hat{v} \cdot -\hat{g}$ . Summing up all visible surface elements of the secondary and the accretion disk, we obtain the total flux spectrum as

$$F(\lambda) = \sum_i \Delta F_i(\lambda)$$

The flux observed through a filter is computed as

$$F = \int F(\lambda)T(\lambda)d\lambda$$

and the magnitude is computed as

$$m = -2.5 \lg(F/F_0)$$

Here  $T(\lambda)$  is the filter transmission, and  $F_0$  is the zeroth magnitude flux, which are taken from the `stdas.synphot` package. In our model illustration, we calculate the magnitudes for Johnson *UBV*, Cousins *RI*, and Bessel *JHK*, but any number of filters can be easily added into the code.

Given the model parameters, the model first sets up the binary geometry, computes the secondary and disk temperature profiles with and without X-ray irradiation, then computes the emergent spectrum and the magnitudes for a binary phase  $\Phi$ . For each binary phase, we put the model output in one figure as shown in Figure 1 for a base model with  $M_\bullet = 30M_\odot$ , a B0V secondary ( $M_* = 17.5M_\odot$ ,  $R_* = 7.4R_\odot$ , and  $T_* = 30,000$  K with solar abundance) filling its Roche lobe ( $f_R = 1$ ),  $L_X = 10^{39}$  erg s $^{-1}$ ,  $X_h = 1$ ,  $X_d = 0.5$ ,  $\beta = 0.5$ ,  $\gamma = 0.5$ , and  $\Theta = 60^\circ$ . In such a figure, the upper left panel shows the binary components projected on the plane normal to the viewing vector  $\hat{v}$ , and the upper right panel shows the *UBVRIJHK* light curves for a whole period with the magnitudes marked for this phase. The lower panel shows the emergent spectra from the secondary with and without X-ray irradiation, from the disk itself and the X-ray irradiation contribution, and from the binary as a whole. As an illustrative product for a given model, we create an animated movie by stacking up a sequence of such figures for binary phases over a period.

## A.6. Dependence on Key Parameters

To illustrate how the model depends on the key parameters, we start from the base model shown in Figure 1. In such a model, the star contributes 70%-60% of the light in the U-I bands, the un-X-ray-irradiated disk contributes 15%-20%, and the X-ray irradiation of the disk contributes the rest 15%-20%. X-ray heating of the L1 side of the secondary boosts it to be the hottest side, yielding a sinusoidal light curve instead of an ellipsoidal one. We vary one parameter in its reasonable range with all other parameters fixed at the base model, and investigate the according changes in the spectrum, the magnitudes, the light curve shapes and variation amplitudes with respect to the base model.

We first investigate the five parameters on X-ray irradiation. The X-ray luminosity is varied from  $10^{38}$  to  $10^{41}$  erg s $^{-1}$ . With increasing X-ray luminosity, the X-ray heated disk and

the L1 side of the secondary become hotter and brighter. Accordingly, the light curve shape changes from ellipsoidal to sinusoidal, with brighter mean magnitudes and larger variation amplitudes. The effects are illustrated in Figure B1.

The disk fattening factor is varied from 0.1 to 10. With increasing fattening, the disk becomes thicker and intercepts more X-ray radiation, thus becomes slightly brighter. The disk casts a larger shadow on the secondary, and the secondary becomes less X-ray heated. Accordingly, the light curve shape changes from sinusoidal to ellipsoidal, with slightly brighter mean magnitudes but smaller variation amplitudes. The effects are illustrated in Figure B2.

The disk size factor is varied from 0.01 to 1. With a larger radius and emitting area, the disk contributes slightly more in the optical, leading to slightly brighter mean magnitudes for the light curves. The slightly larger disk shadow on the secondary reduces the X-ray heating only slightly, and the light curve shape remains sinusoidal yet with smaller variation amplitudes. The effects are illustrated in Figure B3.

The albedo for the disk surface is varied from 0.01 to 0.99. The increasing albedo reduces the heating of the disk, leading to much smaller contribution from the X-ray irradiation of the disk. X-ray heating of the secondary remains the same, and the light curve shape remains sinusoidal. The light curve mean magnitudes decrease slightly, and the variation amplitudes increase slightly, both due to the diminishing of the X-ray irradiation of the disk. The effects are illustrated in Figure B4.

The X-ray to thermal conversion factor is varied from 0.01 to 0.99. We do not link this factor to the disk albedo because the secondary albedo may be different due to temperature and ionization differences, and some of the X-ray energy may be converted to kinetic energy of the materials blown away from the secondary surface. With increasing conversion efficiency, the L1 side of the secondary becomes hotter. The light curve shape changes from ellipsoidal to sinusoidal with slightly brighter mean magnitudes and much larger variation amplitudes. The effects are illustrated in Figure B5.

Now we investigate the parameters that affect the binary configuration. The black hole mass is varied from  $3M_{\odot}$  to  $3000M_{\odot}$ . With the increasing black hole mass, the Roche lobe of the black hole gets larger, the separation gets larger, and the secondary star is less distorted and less gravitationally darkened. The heating of the secondary becomes less and less significant so that the light curves change from sinusoidal to ellipsoidal as illustrated in Figure B6a. Because the secondary star is less gravitationally darkened at higher black hole mass, the variation amplitudes for the light curves become smaller and smaller (Figure B6b). With a fixed disk size factor, the physical size of the disk gets larger at higher black hole mass, and its contribution in the optical gets higher as illustrated in Figure B6a. This also leads

to higher total optical light, and brighter mean magnitudes of the light curves (Figure B6b). At black hole mass  $\leq 10M_{\odot}$ , the separation becomes so small that the secondary star and the disk begin to block each other when they line up, leading to extra shallow drops in the light curves around phases  $0^{\circ}$  and  $180^{\circ}$  (Figure B6a).

The fraction the secondary fills its Roche lobe is varied from 0.01 to 1. With a smaller filling fraction and a fixed secondary, the Roche lobe of the secondary becomes larger. Subsequently, the separation, the Roche lobe of the black hole, and the physical size of the accretion disk all become larger. The larger disk contributes more in the optical, leading to brighter mean magnitudes of the light curves, more so at longer wavelengths. X-ray heating of the secondary becomes less significant, and the light curve shape changes from sinusoidal to ellipsoidal with reduced variation amplitudes. The tidal distortion and gravitational darkening of the secondary also become less significant, adding to the decrease of the variation amplitudes. The effects are illustrated in Figure B7.

The inclination angle is varied from  $0^{\circ}$  (face-on) to  $90^{\circ}$  (edge-on). With the inclination angle increasing, the projected area of the disk becomes smaller, leading to smaller disk contribution in the optical, and dimmer mean magnitudes of the light curves. The projected area of the L1 side of the secondary also becomes larger, leading to larger variation amplitudes for the sinusoidal light curves. When the inclination angle increases to  $70^{\circ}$ , the disk begins to block parts of the secondary, which enhances the contrast between the heated side and its antipodal side, and leads to much larger variation amplitudes. When the inclination angle increases to above  $80^{\circ}$ , the disk begins to block the hottest part of the L1 side of the secondary, which lowers the contrast between the heated side and its antipodal side, and leads to reduced variation amplitudes. The effects are illustrated in Figure B8.

We experiment with the secondary properties by varying spectral types and luminosity classes as listed in Table B1. The quoted mass, radius and temperature are taken from the MK spectral type calibration (Cox 2000) for stars in the solar neighborhood. For main sequence stars, later spectral types are less massive and smaller in size, with higher densities, lower temperatures and lower luminosities. For an O star secondary, the separation is the largest, and X-ray heating of the secondary is a minor effect, leading to an ellipsoidal light curve. X-ray heating becomes significant for a B star secondary, and the light curve becomes sinusoidal with much larger variation amplitude. For still later stellar types, the variation amplitudes become smaller despite the smaller separations and more significant X-ray heating effects, because the accretion disk contribution to the optical light exceeds the star contribution by larger and larger factors. The effects are illustrated in Figure B9.

For supergiant stars, later spectral types are less massive yet larger in size, with lower densities and lower temperatures. For a B5I supergiant with a high temperature, X-ray

Table 1. Model parameters for best cases<sup>a</sup>

model	$\chi^2$	$M_{bh}$	age	$M_{*,ini}$	$M_*$	$R_*$	$T_*$	$f_R$	$\theta$	$L_{38}$	$X_h$	$X_d$	$\beta$	$\gamma$	E(B-V)	$P$	$K'$
A1	70.88	45.3	5.0	44.10	16.99	5.1	71099	0.22	82	163	1.0	0.05	1.00	0.86	0.11	150.1	124
B1	54.94	15.3	39.8	8.08	8.07	9.0	18462	0.54	38	120	6.3	0.18	0.48	0.74	0.11	145.8	71
F1	61.26	6.7	146.8	4.28	4.27	10.6	9505	1.00	56	187	7.3	0.40	0.73	0.65	0.11	146.3	84
A2	84.01	126.4	5.6	37.22	15.99	5.3	65950	0.24	84	113	1.0	0.06	0.72	0.67	0.11	143.1	68
B2	51.91	39.1	50.0	7.18	7.16	8.2	17500	0.51	46	124	4.9	0.14	0.02	0.32	0.11	143.0	47
F2	55.84	8.2	196.0	3.75	3.74	9.9	8695	0.99	38	91	6.1	0.30	0.27	0.14	0.11	143.0	52
A3	96.53	4.5	4.1	57.94	25.66	3.1	98108	0.10	3	277	5.3	0.18	0.07	0.79	0.11	149.0	18
B3	52.43	275.1	39.7	8.09	8.08	7.9	20259	0.44	74	131	4.4	0.12	0.51	0.82	0.11	147.4	21
B3b	53.01	5.9	39.8	8.08	8.07	8.0	19864	0.45	9	148	2.4	0.18	0.59	0.96	0.11	147.6	26
F3	53.89	6.1	217.0	3.58	3.57	9.8	8190	1.00	15	162	6.0	0.28	0.88	0.89	0.11	143.0	24

<sup>a</sup>The columns are (1) model as named in text, (2)  $\chi^2$ , (3) black hole mass in  $M_\odot$ , (4) secondary age in Myrs, (5) initial mass in  $M_\odot$ , (6) current mass, (7) current radius in  $R_\odot$ , (8) stellar temperature, (9) filling fraction the secondary fills its Roche lobe, (10) viewing angle, (11) X-ray luminosity in  $10^{38}$  erg/s, (12) disk fattening factor, (13) disk size in unit of tidal disruption radius, (14) disk albedo, (15) X-ray to thermal conversion factor on secondary surface, (16) E(B-V), (17) period in hours, and (18) black hole radial velocity semi-amplitude when viewed edge-on.

SpType	Mass ( $M_\odot$ )	Radius ( $R_\odot$ )	Temp (K)
O5V	60	12	42000
B5V	5.9	3.9	15200
A5V	2.0	2.4	8180
F5V	1.4	1.3	6650
G5V	0.92	0.92	5560
B5I	20	50	13600
A5I	13	60	8610
F5I	10	100	6370
G5I	12	150	4930

Table A1: Experimented secondary spectral types.

heating of the L1 side of the secondary is not enough to raise it to be the hottest side, and the light curve is an ellipsoidal one. For later spectral types with much lower temperatures, X-ray heating is enough to raise the L1 side of the secondary to be the hottest side, and the light curves become sinusoidal. The physical disk size, along with the Roche lobe of the black hole, becomes larger for later spectral types. Because of its low temperature, the expanded outer disk does not contribute much to the optical at shorter wavelengths (U/B bands), but contributes significantly at longer wavelengths. In the U/B bands, the mean magnitudes of the light curves become dimmer for later spectral types because the secondary becomes dimmer while the disk contribution remains largely the same. In the V–K bands, the mean magnitudes become brighter for later spectral types, more so in the redder bands, because both the disk and the secondary become brighter. The effects are illustrated in Figure B10.

To summarize, five parameters are required to set up the binary model without X-ray irradiation: (1) the black hole mass  $M_{\bullet}$ , (2-3) the secondary mass ( $M_*$ ), radius ( $R_*$ ) and temperature ( $T_*$ ) as determined by its initial mass and age, (4) the fraction  $f_R$  the secondary fills its Roche lobe, and (5) the inclination angle  $\Theta$ . Five extra parameters are required to incorporate the X-ray irradiation: (6) the X-ray luminosity  $L_X$ , (7) the disk fattening factor  $X_h$ , (8) the disk size factor  $X_d$ , (9) the disk albedo  $\beta$ , and (10) the X-ray to thermal conversion factor  $\gamma$ . In total, 10 key parameters are required to fully describe an X-ray irradiated binary model for ULXs.

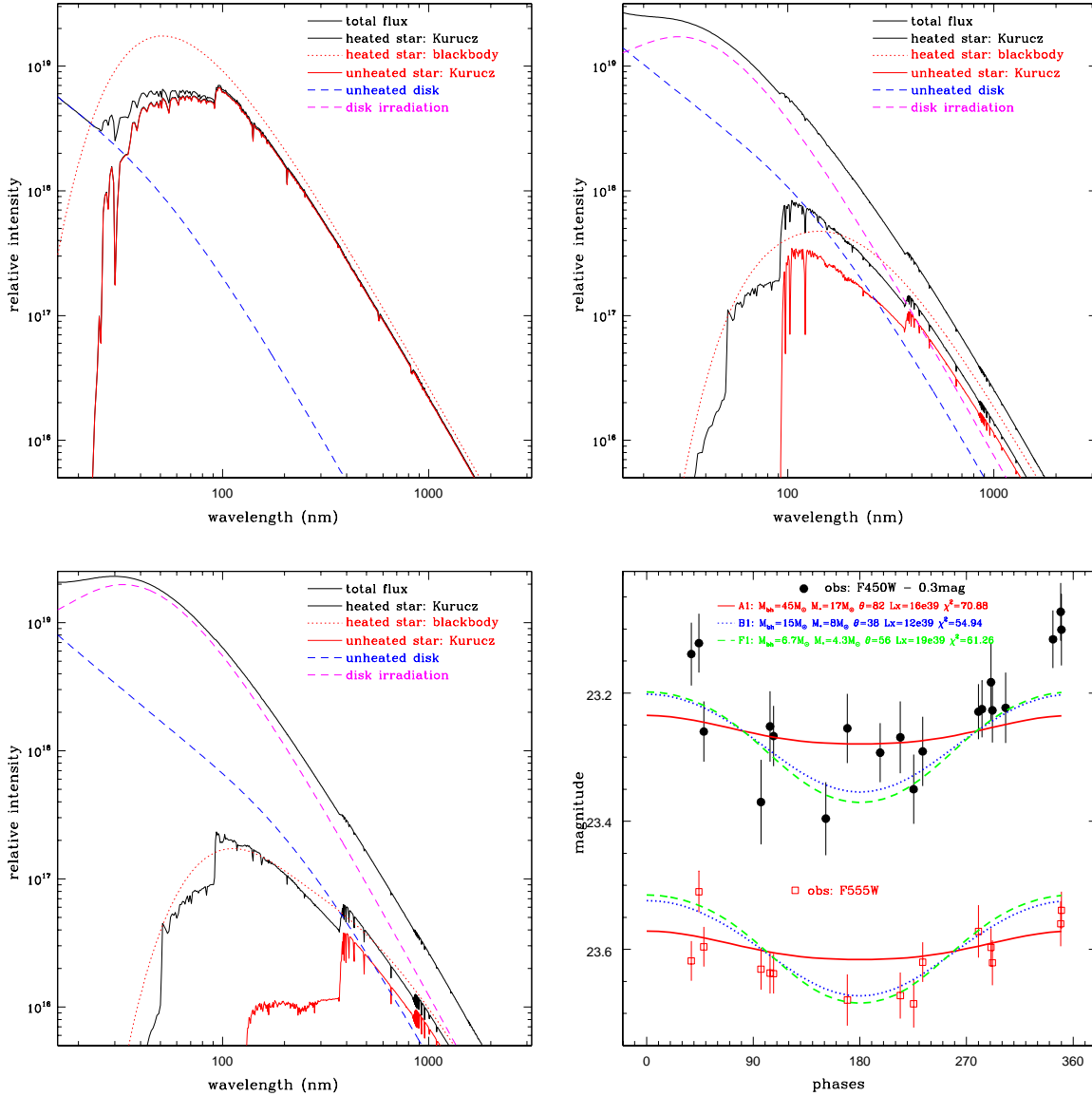


Fig. 5.— (a) The emergent spectrum from model A1 at binary phase  $90^\circ$ . The spectrum is dominated by the hot secondary that is hardly affected by the X-ray heating. (b) The emergent spectrum from model B1 at binary phase  $90^\circ$ . The secondary and the disk contribute roughly equally to the emergent spectrum at  $4000\text{\AA}$ , while the secondary/disk contributes slightly more at longer/shorter wavelengths. The X-ray heating boosts the secondary light by  $>30\%$ . (c) The emergent spectrum from model F1 at binary phase  $90^\circ$ . The spectrum is dominated by the X-ray heated accretion disk, which contributes four times more light than the X-ray heated secondary at  $4000\text{\AA}$ . The X-ray heating boosts the secondary light by  $>60\%$ . (d) The predicted light curves for model A1 (red solid), model B1 (blue dotted line) and model F1 (green dashed line) with HST/WFPC2 F450W/F555W observations overplotted.

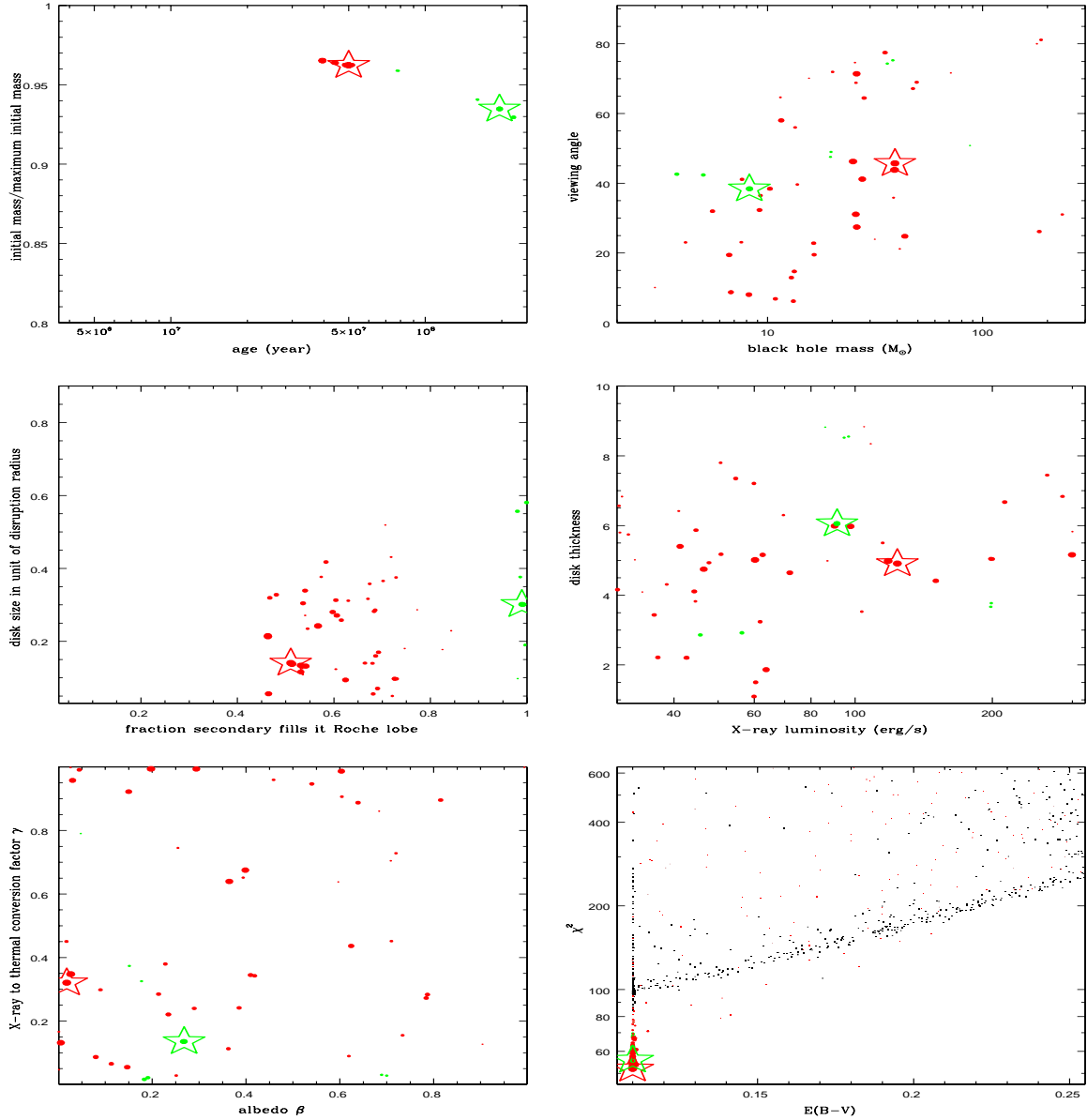


Fig. 6.— Models with  $\chi^2 < 78$  obtained with two rounds of AMOEB searches for assumed  $2K' = 100 \pm 40$  km/s. The symbols are the same as in Figure 4. The asterisks are for model B2 (red) and model F2 (green) as described in the text. The six panels show (a) the secondary age vs initial mass, (b) the black hole mass vs inclination angle, (c) the fraction the secondary fills its Roche lobe vs the disk size in unit of disruption radius, (d) the X-ray luminosity vs the disk thickness, (e) the disk surface albedo vs the X-ray-to-thermal conversion factor on the secondary surface, and (f) the extinction  $E(B-V)$  vs the model  $\chi^2$  for models with  $\chi^2 < 600$ .

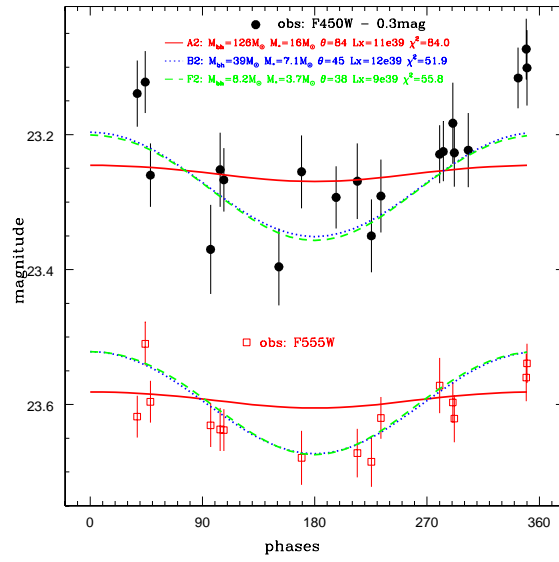


Fig. 7.— The predicted light curves for model B2 (blue dotted line) and model F2 (green dashed line) with HST/WFPC2 F450W/F555W observations overplotted.

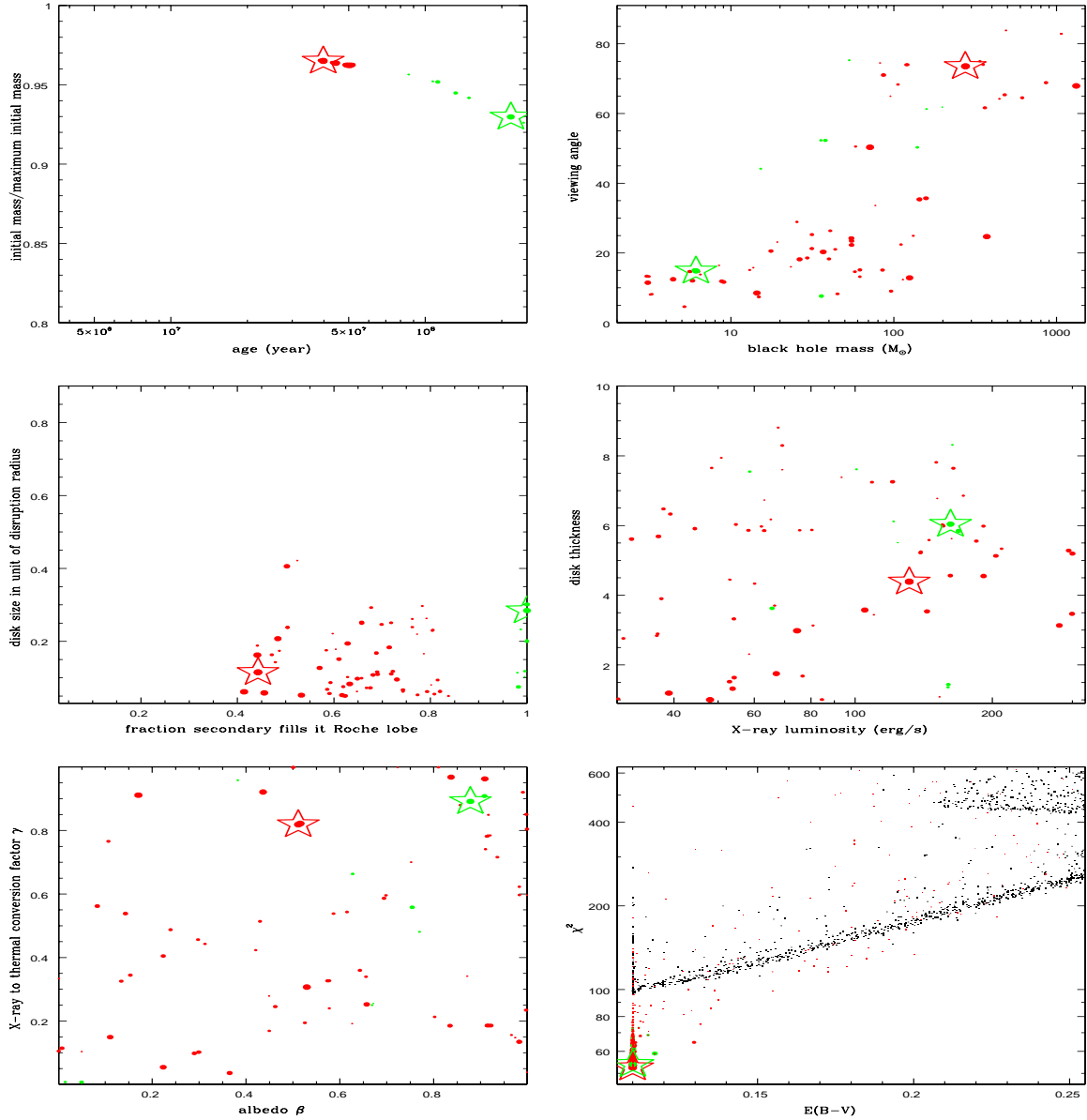


Fig. 8.— Models with  $\chi^2 < 78$  obtained with two rounds of AMOEBA searches for assumed  $2K' = 25 \pm 15$  km/s. The symbols are the same as in Figure 4. The asterisks are for model B3 (red) and model F3 (green) as described in the text. The six panels show (a) the secondary age vs initial mass, (b) the black hole mass vs inclination angle, (c) the fraction the secondary fills its Roche lobe vs the disk size in unit of disruption radius, (d) the X-ray luminosity vs the disk thickness, (e) the disk surface albedo vs the X-ray-to-thermal conversion factor on the secondary surface, and (f) the extinction  $E(B-V)$  vs the model  $\chi^2$  for models with  $\chi^2 < 600$ .

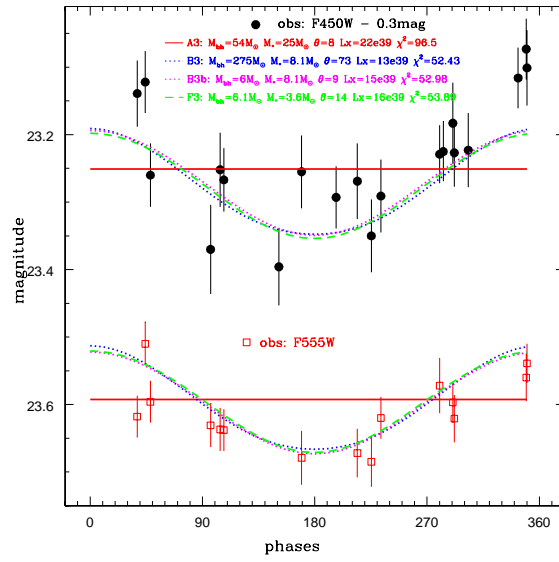


Fig. 9.— The predicted light curves for model B3 (blue dotted line) and model F3 (green dashed line) with HST/WFPC2 F450W/F555W observations overplotted.

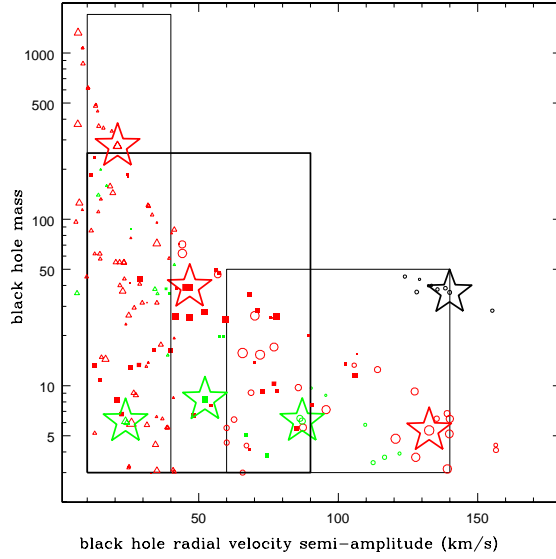


Fig. 10.— The black hole radial velocity semi-amplitude versus black hole mass for acceptable models with  $\chi^2 < 78$  for the cases of  $K' = 100 \pm 40$  km/s (open circles),  $K' = 50 \pm 40$  km/s (filled squares) and  $K' = 25 \pm 15$  km/s (open triangles). The symbol sizes are inversely scaled with the  $\chi^2$  values of the models. The asterisks are the best models for groups one (black), two (red) and three (green) as described in the text. The three boxes indicate the rough ranges of “acceptable” models for three cases.

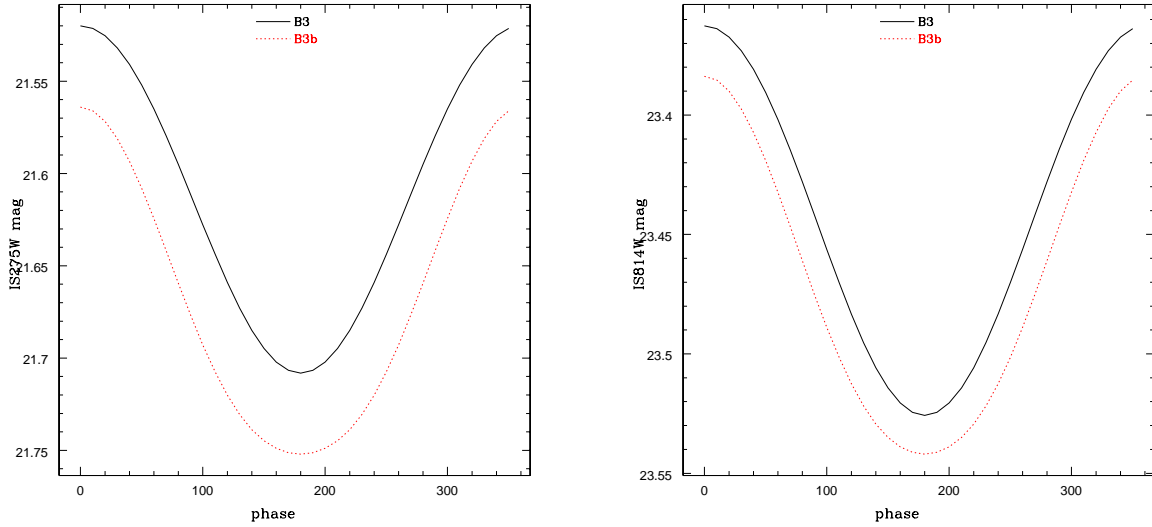


Fig. 11.— The predicted HST WFC3/UVIS F275W and F814W light curves for the two models B3 and B3b for  $K' \sim 20$  km/s.

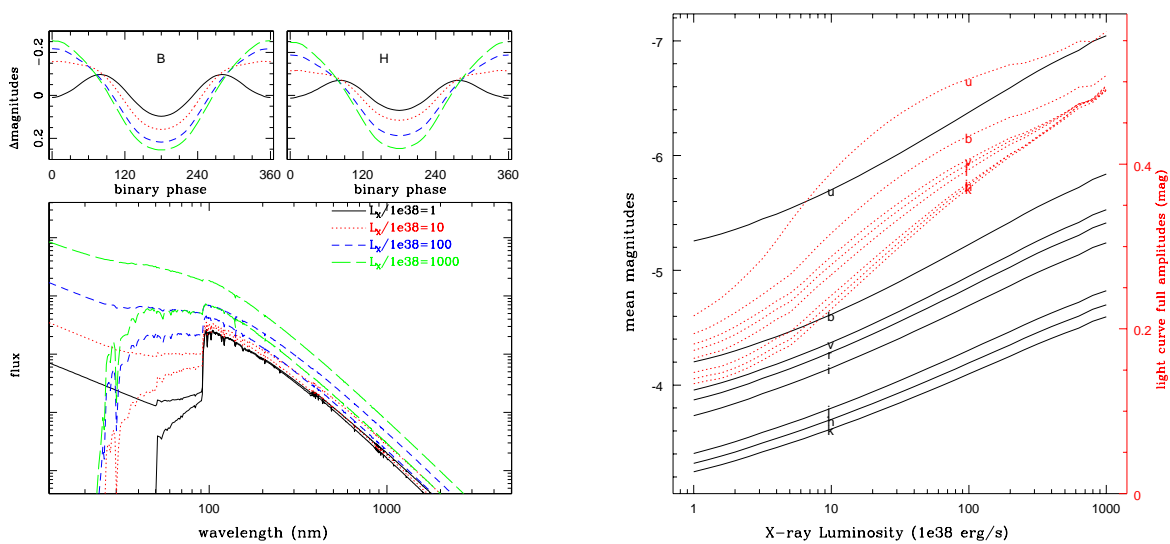


Fig. A1.— (a) The spectra (lower panel) and the B/H light curves (upper panel) for models with different X-ray luminosities. The thin spectra are for the X-ray heated star, and the thick spectra are for the sum of the star and the disk. (b) The mean magnitudes (solid) and the variation amplitudes (dotted) of the UBVR IJHK light curves for models with different X-ray luminosities.

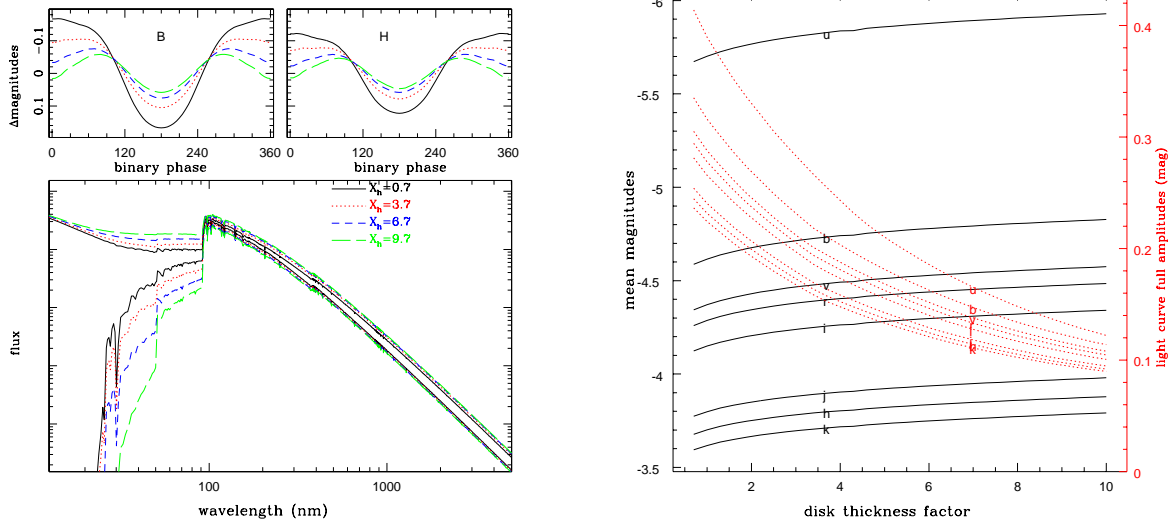


Fig. A2.— (a) The spectra (lower panel) and the B/H light curves (upper panel) for models with different disk fattening factors. The thin spectra are for the X-ray heated star, and the thick spectra are for the sum of the star and the disk. (b) The mean magnitudes (solid) and the variation amplitudes (dotted) of the UBVRIJHK light curves for models with different disk fattening factors.

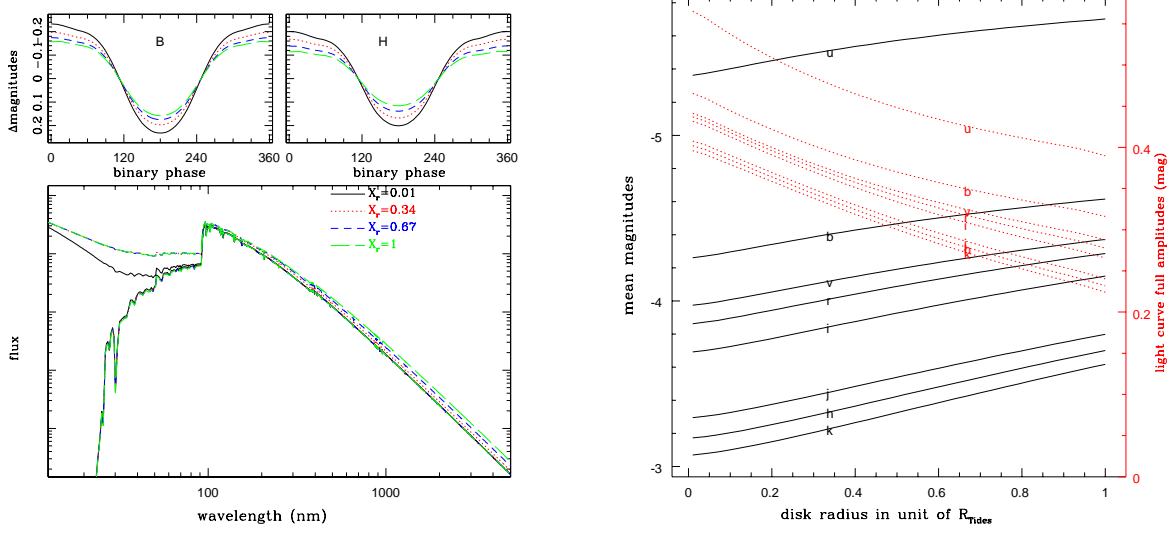


Fig. A3.— (a) The spectra (lower panel) and the B/H light curves (upper panel) for models with different disk size factors. The thin spectra are for the X-ray heated star, and the thick spectra are for the sum of the star and the disk. (b) The mean magnitudes (solid) and the variation amplitudes (dotted) of the UBVRIJHK light curves for models with different disk size factors.

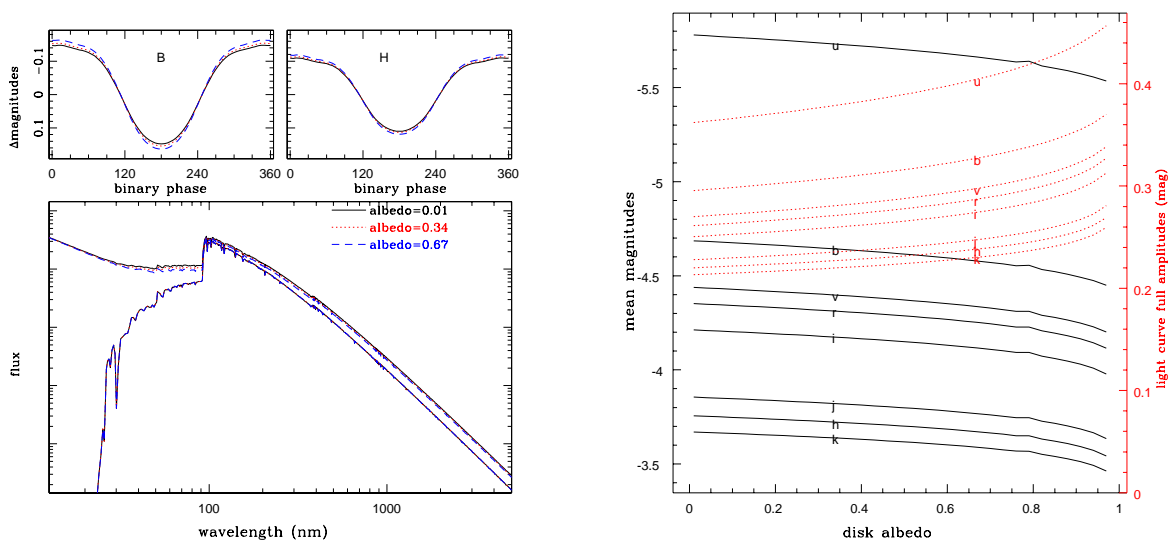


Fig. A4.— (a) The spectra (lower panel) and the B/H light curves (upper panel) for models with different disk albedo. The thin spectra are for the X-ray heated star, and the thick spectra are for the sum of the star and the disk. (b) The mean magnitudes (solid) and the variation amplitudes (dotted) of the UBVRIJHK light curves for models with different disk albedo.

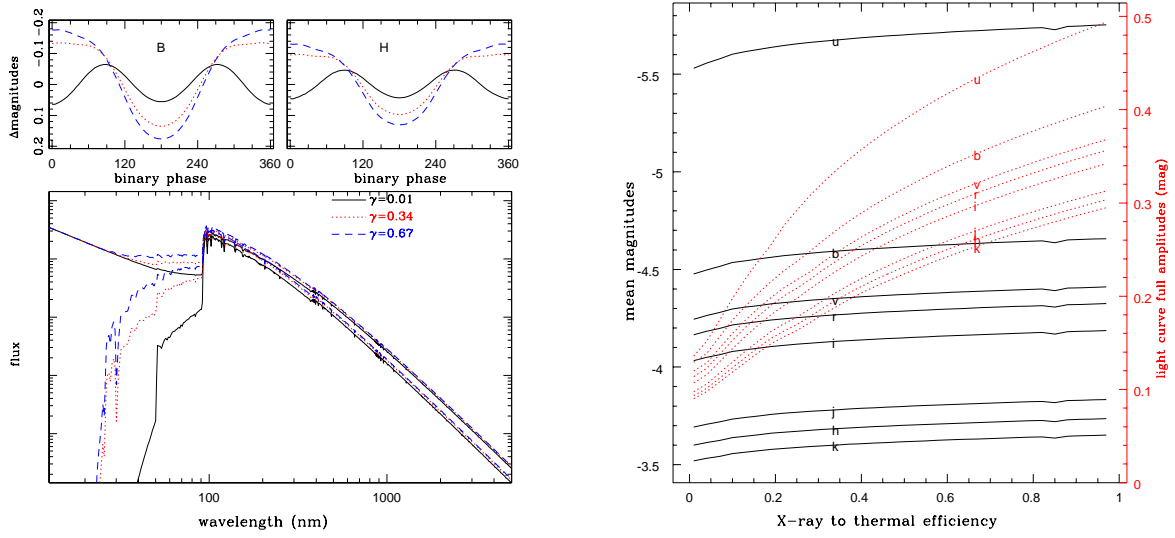


Fig. A5.— (a) The spectra (lower panel) and the B/H light curves (upper panel) for models with different X-ray to thermal conversion factor on the secondary surface. The thin spectra are for the X-ray heated star, and the thick spectra are for the sum of the star and the disk. (b) The mean magnitudes (solid) and the variation amplitudes (dotted) of the UBVRIJHK light curves for models with different X-ray to thermal conversion factor on the secondary surface.

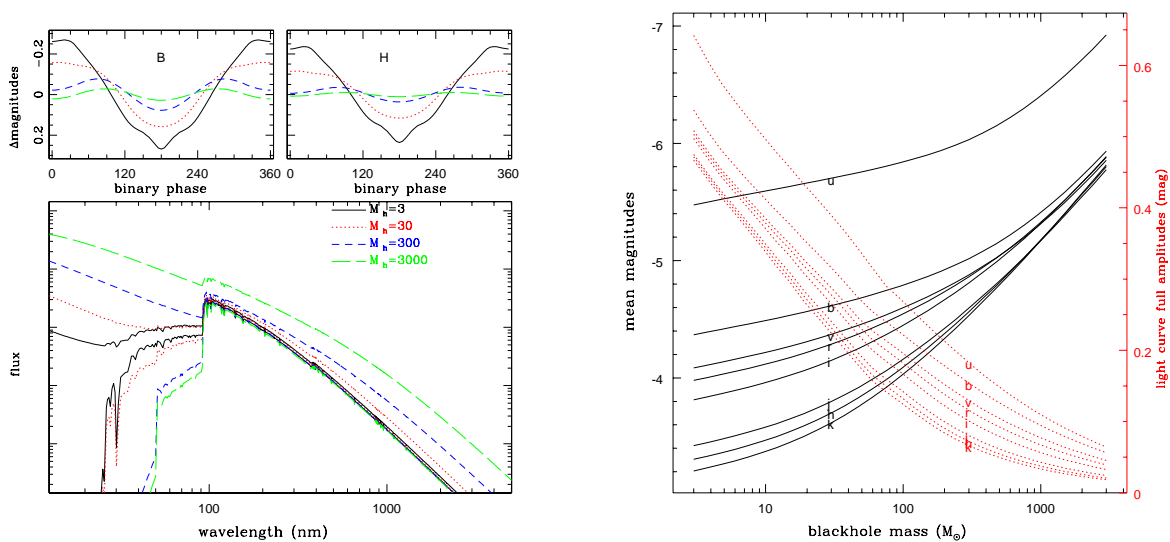


Fig. A6.— (a) The spectra (lower panel) and the B/H light curves (upper panel) for models with different black hole masses. The thin spectra are for the X-ray heated star, and the thick spectra are for the sum of the star and the disk. (b) The mean magnitudes (solid) and the variation amplitudes (dotted) of the UBVRIJHK light curves for models with different black hole masses.

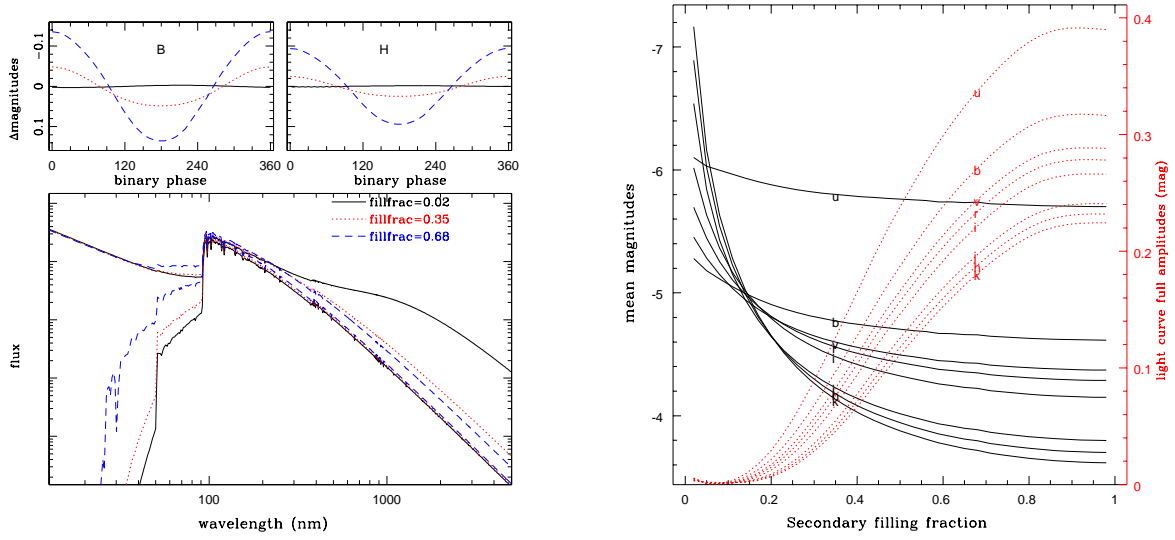


Fig. A7.— (a) The spectra (lower panel) and the B/H light curves (upper panel) for models with different fractions the secondary fills its Roche lobe. The thin spectra are for the X-ray heated star, and the thick spectra are for the sum of the star and the disk. (b) The mean magnitudes (solid) and the variation amplitudes (dotted) of the UBVRIJK light curves for models with different fractions the secondary fills its Roche lobe.

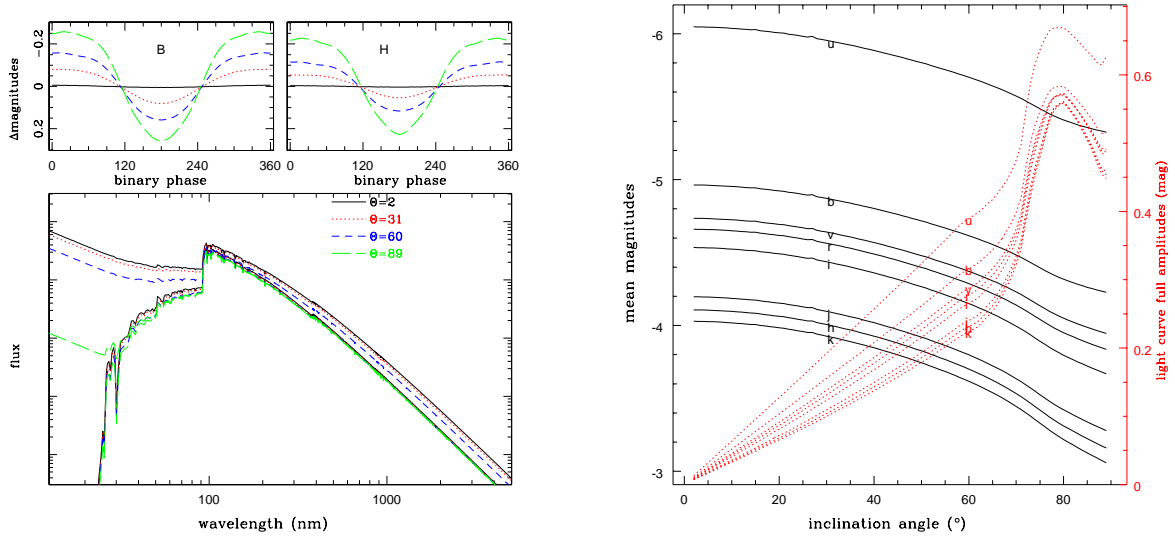


Fig. A8.— (a) The spectra (lower panel) and the B/H light curves (upper panel) for models with different inclination angles. The thin spectra are for the X-ray heated star, and the thick spectra are for the sum of the star and the disk. (b) The mean magnitudes (solid) and the variation amplitudes (dotted) of the UBVRIJHK light curves for models with different inclination angles.

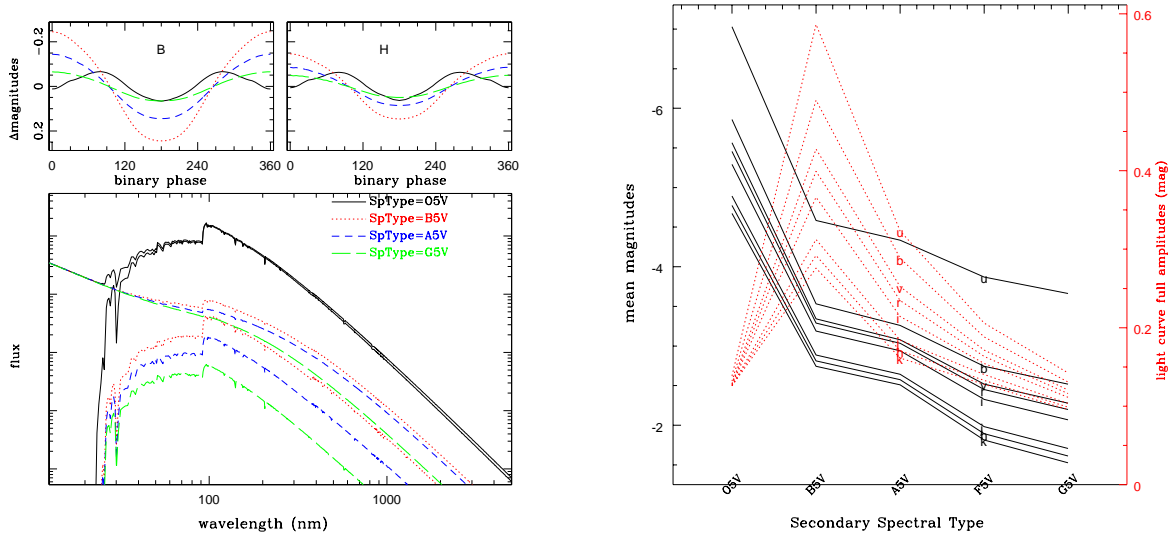
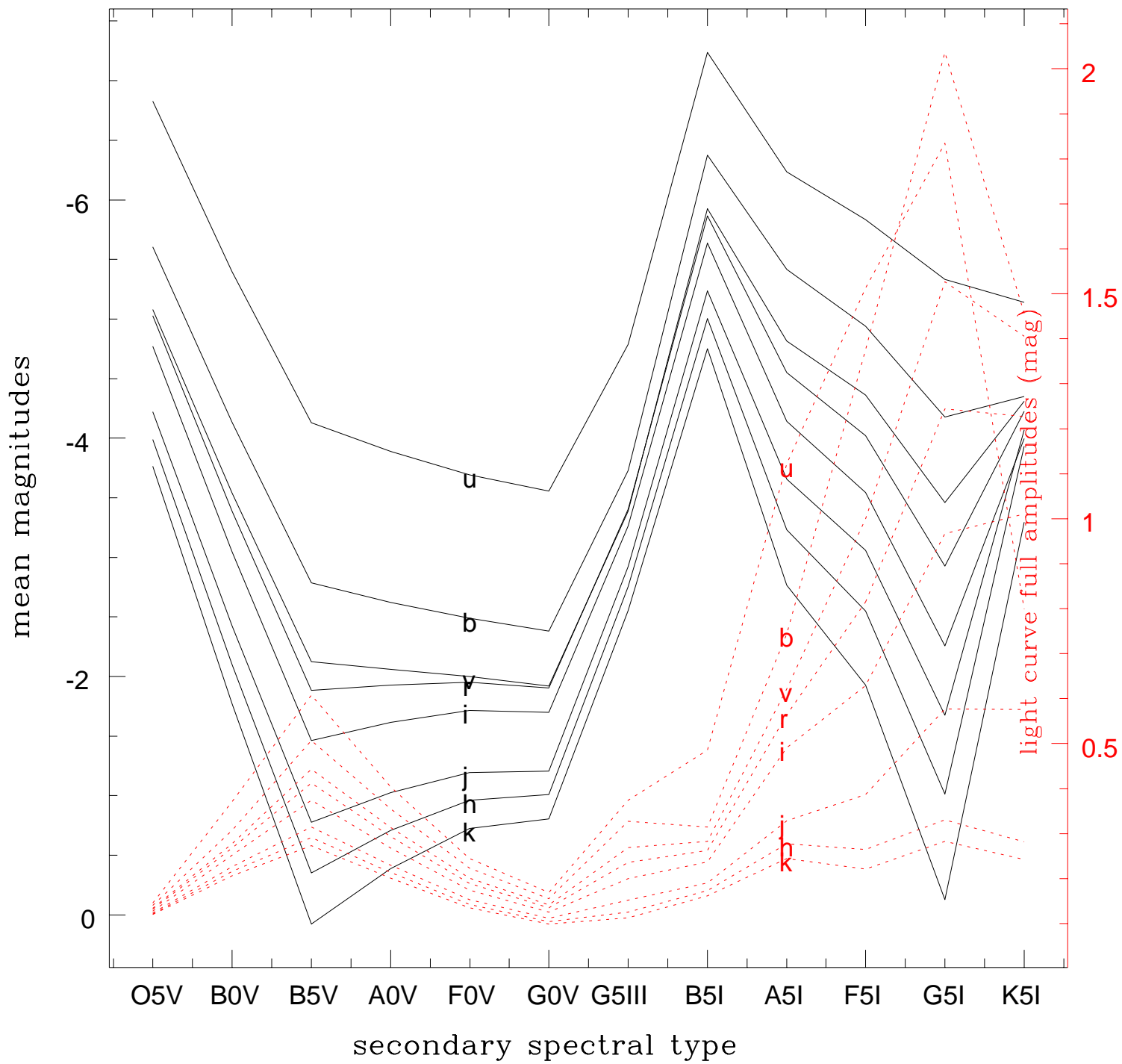


Fig. A9.— (a) The spectra (lower panel) and the B/H light curves (upper panel) for models with dwarf secondaries of different spectral types. The thin spectra are for the X-ray heated star, and the thick spectra are for the sum of the star and the disk. (b) The mean magnitudes (solid) and the variation amplitudes (dotted) of the UBVRIJHK light curves for models with dwarf secondaries of different spectral types.





phase

